THEORETICAL AND EXPERIMENTAL INVESTIGATIONS OF THE PHYSICS OF CRYSTALLINE SURFACES

Principal Investigator: E. Bauer

Annual Report
For the Period February 1, 1966 to January 31, 1967

Prepared for the

National Aeronautics and Space Administration
Washington, D. C.

Fund Transfer R-05-030-001

U. S. Naval Ordnance Test Station
China Lake, California 93555

ANNUAL REPORT ON REQUEST NO. R-09-030-001 FOR THE PERIOD 1 FEBRUARY 1966 THROUGH 31 JANUARY 1967

I. SUMMARY OF WORK

The efforts during the past report year were concentrated on the following problems:

(1) The relation between structure of epitaxial films and surface and interfacial energies.

(2) Quantitative studies of the elastic and inelastic interactions of slow electrons with tungsten single crystal surfaces.

(3) The determination of nature and structure of surface layers with low energy electron diffraction.

(4) The relation between structure and electron emission properties of work function reducing layers on tungsten {110} planes.

(5) Momentum exchange of atoms on well defined single crystal surfaces.

(6) Theory of low energy electron scattering.

The work on problems (2) and (5) was nearly completely concerned with equipment construction, modification and testing. Problems (1) and (4) involved considerable, problem (3) minor equipment improvement. Therefore most of the results were obtained in problem areas (1), (3) and (4).

II. The relation between structure of epitaxial films and surface and interfacial energies (A. K. Green and E. Bauer).

The work during the past year in the area of epitaxy has been a continuation of the effort to contribute to the solution of the problem of the influence of the interface on the epitaxial growth of thin films on well characterized surfaces. The first part of the year was spent in carefully analyzing our recent experimental results and comparing them with other independent work. This effort has been reported in the First and Second Quarterly Reports (see also ref. VIII (2), (4), (5), (7)). Briefly, some of the main results obtained are: (1) The phenomenon of epitaxy is highly specific for each film substrate pair, as exhibited conclusively by simultaneous deposition onto air and vacuum cleaved surfaces of NaCl and KCl. (2) The nucleation rate is significantly less on the vacuum cleaved surface. (3) Several orientations are observed which have not been reported previously. (4) The coalescence stage of the film growth is extremely important and the in situ reflection electron diffraction patterns differ considerably from the results obtained by standard transmission electron diffraction and microscopy of films removed from the substrate. (5) Theoretical considerations as discussed in the Second

Quarterly Report indicate that the phenomenological theory can best account for nucleation but that at present no theory is adequate. The role of interfacial and free surface energies in the coalescence process is emphasized as well as the importance of the twin boundary energy and chemical reactions.

Efforts to study the growth of NaCl on air and vacuum cleaved NaCl produced the preliminary surprising result that twinning occurs preferentially on the (clean) vacuum cleaved side and not on the (contaminated) air cleaved side where it would be expected preferentially. This work has been postponed due to vacuum problems arising from the heavy outgassing of NaCl when heated to evaporation temperature.

The experiments described above and many others show that adsorbed gases play a major role in crystal growth on surfaces. So can impurities diffusing out of the bulk when heated or evolved during cleaving. It is therefore important to understand the gas desorption and evolution processes from alkali halides. Therefore a quantitative study of the gases evolved from NaCl upon linear temperature increase has been started which has produced the following results to date: (1) The major gas being liberated is H_2O. (2) NaCl which has been deliberately exposed to H_2O exhibits large bursts of H_2O in roughly reproducible temperature regions. (3) NaCl which has been freshly cleaved in air exhibits H_2O desorption peaks in roughly the same temperature regions in which bursts from H_2O exposed specimens occur.

III. Quantitative studies of the elastic and inelastic interactions of slow electrons with tungsten single crystal surfaces (J. O. Porteus).

Progress has been made in producing tungsten single crystal surfaces of satisfactory quality for quantitative intensity measurements. The ability to maintain sample cleanliness during the required scanning times was investigated and found to be inadequate with the present oil-diffusion pumping system. Replacement with an electrostatic ion pump is now in progress. Also, an automatic voltage-scanning and beam-tracking system has been developed for rapid intensity vs. voltage measurements. Preliminary intensity vs. voltage measurements of the (00) beam form a W (110) surface have been obtained, along with preliminary inelastic scattering measurements from this surface. Further developments were made in mathematical methods for differentiation and improvement of resolution of the inelastic data (Encl. 2).

IV. The determination of nature and structure of surface layers with low energy electron diffraction (E. Bauer).

The low energy electron diffraction (LEED) studies during the past year can be divided up as follows: (1) A study of specific problems in the growth of f.c.c. metals on alkali halides. (2) The interpretation of complex LEED patterns. (3) A study of the systems Sr-O-C-W.

(1) Two specific problems were studied: (a) The structural differences between air cleaved NaCl surfaces and NaCl surfaces cleaned by heating to 500°C. No difference in the lattice periodicity was found, only the background on the

air cleaved surface was higher indicating random distribution of the "adsorbed" impurities. (b) The correlation between the 1/5 structure observed in reflection electron diffraction (RED) on epitaxial Au films with the LEED (5x1) structure on bulk (100) Au single crystals. No LEED pattern could be obtained from the Au film. In view of the much larger information obtained from RED studies (see I) the LEED experiments were soon terminated.

(2) Many complex LEED patterns have been reported in the literature for surfaces covered with adsorption layers and also for clean surfaces. Most of these patterns have been attributed to complex exotic two-dimensional superstructures. We have suggested previously that many of these patterns are probably produced by double scattering between superimposed well known structures. The experiments to be described below in which many such "superstructure" patterns are observed made it necessary to examine their origin more closely and to develop interpretation techniques. This has been done and illustrated by a number of examples (see Encl. 1).

(3) Most of the LEED effort was concentrated on the study of the system Sr-O-C-W, which turned out to be very complex. It started out with a study of the system SrO-W {110} in connection with the studies of the relation between work function and surface structure (see V). It soon turned out that the low temperature (30-700°C) growth of SrO films and their work function could be understood only if the influence of the major residual gas component, i.e. CO, would be known. Also the formation of complex high temperature reaction products between SrO and W indicated that the high temperature reactions between O_2 and W must be understood first. The study of the SrO system (see ref. VIII (6) for some of the results) thus lead to the study of the systems CO-W {110} and oxygen-W {110}, systems which recently have received much attention for a quite different reason, i.e. because of the controversy regarding surface reconstruction upon adsorption (see ref. VIII (3)). Considerable experimental material has been accummulated during the second half of the report year. However the conclusions which can be drawn from these experiments are so much in contradiction to the generally accepted views not only of CO and O_2 adsorption on W, but also of many other adsorption processes, that we believe a repetition of our experiments and collection of additional experimental evidence is necessary before our conclusions can become acceptable. These conclusions are in short: (1) the strongly bound ß adsorption layers observed in many adsorption systems are not adsorption layers in the classical sense, but thin reaction layers between crystal and gas; (2) the various ß states reported are not due to adsorption on different planes, but correspond to different binding states in the reaction layer on one and the same surface; (3) except at very low temperatures CO adsorption in general leads to carbonyl formation so that a metal surface saturated with CO is covered with a metal carbonyl layer; the species desorbed from such a surface may be to a large extent carbonyl. These conclusions, at least in the case of CO, are correct only if it can be shown that the gas pressure and surface coverage experiments on which the presently accepted views of chemisorption are based are in error by a factor of 3 or more. Experiments planned for the following year should clarify this discrepancy and determine whether our conclusions are correct or not.

V. The relation between structure and electron emission properties of work function reducing layers on W {110} planes (G. Turner and E. Bauer).

During this report year, the primary system under investigation has been SrO-W {110}. The results of this work have shown: (1) a monotonic decrease in work function as a function of film thickness, with no ordered surface structure, for SrO deposited on W {110} at room temperature; (2) a minimum is observed in the work function for increasing annealing temperature of the SrO film together with a definite ordering of the surface structure; (3) as the SrO film is heated, regions of very high photoelectric emission appear which can be correlated with the work function minimum. There is, in general, a very complex dependence of the structure and emission properties of the SrO-W {110} systems upon film thickness, annealing time and temperature, and deposition rate. The results obtained cannot be explained by the dipole-layer theory and for a better understanding other systems must be studied. Late in the year, a study of the BaO-W {110} system was initiated which is still in progress. No results are available at this time. In support of the extension of the investigation, long lived and highly directional evaporation sources have been developed for the alkaline earths and their oxides. Work is continuing on the magnetic deflection system and associated electron optics for the modification of the UHV low energy reflection electron microscope. An improved electron source for the microscope is also being developed in the form of a field emission gun.

VI. Momentum exchange of atoms on well defined single crystal surfaces (W. Faith and E. Bauer).

This project has been in the equipment construction and testing stage during this report year. The equipment combines a molecular beam and a LEED system so that the surface condition of the single crystal specimen can be checked at any moment during the molecular beam experiment. The importance of this is obvious (see the project proposal). The construction of the molecular beam attachment to the LEED system was completed after the first half of the report year. Subsequent testing revealed a major problem, even after improvement of the nozzle design: the pumping speed of the VacIon pumping system for a steady state load of Ar in the 10^{-8} torr range was too slow. As a result the beam flux at the surface was small compared to the random flux and no scattering patterns could be obtained. It was therefore decided towards the end of the report year to build a diffusion pump system for this project, which at the same time will extend the versatility of the experiments: it will also allow study of the momentum exchange of He and of other gases poorly pumped by VacIon pumps. This work is still in progress.

VII. Theory of low energy electron scattering (E. Bauer).

Little effort and consequently little progress was made in this area during this report year. The work on relativistic effects was continued, mainly to obtain an understanding of the magnitude of the influence of exchange and polarization. Polarization was found to be unimportant down

to about 1 eV for Hg, but the influence of exchange as expressed by the condition of orthogonality of bound and free electron wave functions seems to be significant according to preliminary calculations. Work on developing efficient techniques for the calculations of scattering phases by atoms and ions has continued. The theory of diffraction by crystals has been developed in the second Born approximation to the stage ready for programming. Numerical calculations are planned for the following year.

VIII. Publications

1. "Importance of Relativistic Effects in the Scattering of Slow Electrons," by H. N. Browne and E. Bauer, Phys. Rev. Letters 16, 495 (1966).

2. "On the Epitaxial Growth of Single-Crystal Metal Films Free of Impurities," by E. Bauer, A. K. Green, and K. M. Kunz, Appl. Phys. Letters 8, 248 (1966).

3. 'Comments on the "Uncertainty Regarding Reconstructed Surfaces" by L. H. Germer', by E. Bauer, Surface Science 5, 152 (1966).

4. "The Formation of Thin Continuous Films from Isolated Nuclei," by E. Bauer, A. K. Green, K. M. Kunz, and H. Poppa, in Basic Problems of Thin Film Physics, ed. by R. Niedermayer and H. Mayer. Göttingen, Vanderhoeck & Ruprecht, 1966, p. 135.

5. "On the Formation of Single Crystal Films of f.c.c. Metals on Alkali Halide Cleavage Planes in Ultrahigh Vacuum" by K. M. Kunz, A. K. Green and E. Bauer, phys. stat. sol. 18, 441 (1966).

6. "An Ultrahigh Vacuum Electron Microscope and Its Applications to Work Function Studies," by G. Turner and E. Bauer, in 6th International Congress Electron Microscopy, Kyoto (1966), Maruzen Co., Tokyo 1966, p. 163.

7. "On the Formation of Single-Crystal Films of f.c.c. Metals on Alkali Halide Cleavage Planes," by E. Bauer and A. K. Green, submitted to Z. Kristallogr.

8. "Multiple Scattering Versus Superstructures in Low Energy Electron Diffraction," by E. Bauer, to be submitted to Surface Science.

9. "Linear Unfolding Methods and Optimization for X-ray and Similar Spectra," by J. O. Porteus, to be submitted to J. Appl. Phys.

Multiple Scattering Versus Superstructures in Low Energy Electron Diffraction

E. Bauer
Michelson Laboratory, China Lake, California, 93555, U.S.A.

LEED patterns indicating a long periodicity of the surface layer are discussed in terms of double scattering between short-period structures occurring in the bulk. It is shown that the geometry of the diffraction pattern does not permit a distinction between a true two-dimensional superstructure and superposed two- or three-dimensional structures ("pseudo-superstructure") giving rise to the same lateral periodicity as the superstructure. Several examples for such pseudo-superstructures are given.

I. INTRODUCTION

Although the importance of multiple scattering in LEED has been pointed out[1,2] and applied to complex diffraction patterns[3] some time ago, most of the more complicated LEED patterns reported to date--with a few exceptions, e.g. for NiO on the {111} Ni plane[4] or for Cu on the W {110} plane[5]--have been explained in terms of single scattering, leading to complex two-dimensional surface structures commensurate with the complexity of the diffraction patterns. This limited use of the multiple scattering interpretation is in part due to a misconception of the diffraction process and in part a consequence of the expectation that surfaces have a tendency to form complicated two-dimensional structures.[6] It is the purpose of

this paper to correct this misconception (Sect. II) and to illustrate with a few examples that the complex LEED patterns can be interpreted in terms of multiple scattering by superimposed well known structures (Fig. 1b) so that no exotic two-dimensional surface structures (Fig. 1a) have to be assumed (Sect. III).

II. THEORY

The misconception mentioned is based on an oversimplified picture of the diffraction process as illustrated in Fig. 2a, which shows a section normal to the surface through the superposed reciprocal lattices of two crystals with different lattice constants. It is assumed that double scattering requires the possibility of diffraction in each crystal individually, i.e. the Ewald sphere must pass through both sets of reciprocal lattice rods. As a consequence, significant multiple scattering should not occur for energies below 10-20 eV, where the Ewald sphere is too small to fulfill this condition. If a large periodicity is observed at such low voltages it is concluded that the pattern is produced by a real two-dimensional surface structure with long periodicity. This conclusion seems to be supported by the widely accepted assumption of a negligible penetration depth of such slow electrons. This assumption however is contradicted by photoelectric measurements which indicate that even slower electrons than those used in LEED can penetrate several atomic layers. Unless one invokes a Ramsauer-Townsend effect even the slowest electrons used in LEED should therefore be able to penetrate several atomic layers. The basic picture of the scattering process as outlined above is based on the erroneous assumption that the diffraction process can be divided up into well

defined scattering processes in the two different crystals. Actually, the scatterer consisting of the superimposed crystals responds as a whole to the incident wave and reflects waves corresponding to all periodicities within the scatterer including that produced by the superposition of the crystal. The Ewald construction must therefore be performed in the reciprocal lattice of the pseudosuperstructure (Fig. 2b) formed by the two superimposed crystals (Fig. 1b) just as if there were a real two-dimensional long periodicity structure on the surface (Fig. 1a). Consequently, the appearance at very low energies of a LEED pattern corresponding to a "superstructure" does not permit distinction between the surface structures illustrated in Fig. 1.

This can be seen in the following manner: The scattering amplitude of the scattering volume Ω at large distance is given by

$$f = -\frac{1}{4\pi} \int_{\Omega} e^{-i\underset{\sim}{k}\cdot\underset{\sim}{r}'} U(\underset{\sim}{r}')\psi(\underset{\sim}{r}')d\underset{\sim}{r}' \qquad (1)$$

where $\psi(\underset{\sim}{r}')$ is the wave function of the electron involved in the scattering process in the scatterer and $U(\underset{\sim}{r}')$ is the scattering potential. If the lateral periodicity of the "superstructure" formed by the superposition of the two different lattices with the unit cell dimensions $\underset{\sim}{a}_1$, $\underset{\sim}{a}_2$ and $\underset{\sim}{b}_1$, $\underset{\sim}{b}_2$ parallel to the surface is given by the vectors $\underset{\sim}{c}_1 = A_{11}\,\underset{\sim}{a}_1 + A_{12}\,\underset{\sim}{a}_2 = B_{11}\,\underset{\sim}{b}_1 + B_{12}\,\underset{\sim}{b}_2$ and $\underset{\sim}{c}_2 = A_{21}\,\underset{\sim}{a}_1 + A_{22}\,\underset{\sim}{a}_2 = B_{21}\,\underset{\sim}{b}_1 + B_{22}\,\underset{\sim}{b}_2$, then for any point $\underset{\sim}{r}' = \underset{\sim}{r}'_o + m_1\,\underset{\sim}{c}_1 + m_2\,\underset{\sim}{c}_2$

$$U(\underset{\sim}{r}'_o + m_1\,\underset{\sim}{c}_1 + m_2\,\underset{\sim}{c}_2) = U(\underset{\sim}{r}'_o) \quad , \qquad (2)$$

where m_1, m_2 are integers. The wave function at equivalent points of the "superstructure" differs only by a phase factor. For an incident plane

wave $\psi_o = e^{i\underset{\sim}{k}_o \cdot \underset{\sim}{r}}$ we have

$$\psi(\underset{\sim}{r}'_o + m_1 \underset{\sim}{c}_1 + m_2 \underset{\sim}{c}_2) = e^{i\underset{\sim}{k}_o \cdot (m_1 \underset{\sim}{c}_1 + m_2 \underset{\sim}{c}_2)} \psi(\underset{\sim}{r}'_o) \quad . \qquad (3)$$

With (2) and (3) the integration (1) over the whole scattering volume can be broken up into a summation over all "superstructure" unit cells and an integration over the "superstructure" unit cell:

$$f = \left(\sum_{m_1 m_2} e^{-i(\underset{\sim}{k}-\underset{\sim}{k}_o)\cdot(m_1\underset{\sim}{c}_1 + m_2\underset{\sim}{c}_2)} \right) \left(-\frac{1}{4\pi} \int_{\Omega_o} e^{-i\underset{\sim}{k}\cdot\underset{\sim}{r}'_o} U(\underset{\sim}{r}'_o)\psi(\underset{\sim}{r}'_o) d\underset{\sim}{r}'_o \right) = G \cdot F \quad . \quad (4)$$

The intensity distribution of the scattered wave is proportional to $|f|^2 = |G|^2 \, |F|^2$. The "lattice amplitude" G determines the directions of the diffracted waves and the "dynamical structure amplitude" F determines their relative intensities. The integration in F extends over all points within the "superstructure" unit cell which is a column normal to the crystal surface with the cross section $\underset{\sim}{c}_1 \cdot \underset{\sim}{c}_2$ and a height $|\underset{\sim}{c}_3|$ determined by the penetration depth of the electron wave field. At present the calculation of F is only a partially solved problem even for simple structures and will not be considered here. Instead the discussion will be limited to the direction of the diffracted waves, i.e. to the diffraction spot positions on the fluorescent screen, as determined by the lattice amplitude.

The summations over m_1 and m_2 in (4) can be easily performed leading to

$$|G(\underset{\sim}{K})|^2 = \frac{\sin^2 \frac{1}{2} M_1 K_1}{\sin^2 \frac{1}{2} K_1} \frac{\sin^2 \frac{1}{2} M_2 K_2}{\sin^2 \frac{1}{2} K_2} \qquad (5)$$

for a scatterer consisting of $M_1 \cdot M_2$ "superstructure" unit cells. Here

$\underset{\sim}{K} = \underset{\sim}{k} - \underset{\sim}{k}_o$ has been expressed in terms of its components with respect to the axes $\underset{\sim}{c}_i^*$ of the reciprocal lattice of the "superstructure":

$$\underset{\sim}{K} = K_1 \underset{\sim}{c}_1^* + K_2 \underset{\sim}{c}_2^* + K_3 \underset{\sim}{c}_3^*$$

$|G|^2$ has maxima of height $M_1^2 \cdot M_2^2$ whenever $K_i = 2\pi h_i$ (h_i integers), which are very sharp if M_1 and M_2 are large. Strong diffraction will therefore occur when

$$\underset{\sim}{K}^t = \underset{\sim}{k}^t - \underset{\sim}{k}_o^t = 2\pi(h_1 \underset{\sim}{c}_1^* + h_2 \underset{\sim}{c}_2^*) \quad ,$$

i.e. the differences between the tangential components of the incident and reflected wave vectors must be vectors in the reciprocal lattice of the "superstructure". This is true both for real superstructures (Fig. 1b) and apparent superstructures (Fig. 1a), so that the Ewald construction in both cases must be as indicated in Fig. 2b, q.e.d. The distinction between the two cases is possible only by an intensity analysis because the distribution of the atoms within the "superstructure" unit cell which distinguishes the two cases shows up only in the structure amplitude F.

III. PATTERN INTERPRETATION PROCEDURES

The interpretation of "superstructure" patterns is based on the assumption that the pattern is produced by the superposition onto the substrate crystal of a very thin layer of a crystal with a structure and/or orientation different from that of the substrate. With the substrate structure and orientation known the problem is to determine the structure and orientation of the surface layer. It can be solved only with some knowledge of the atomic species present in the surface layer. With this knowledge usually only a small number of crystallographic structures have

to be considered in the interpretation process. For example--to take a complicated case--after the reaction of oxygen with pure tungsten under clean conditions there are less than ten oxide structures corresponding to different oxygen content or different polymorphic forms. A systematic study of the relation between diffraction patterns and experimental conditions--such as the oxygen exposure in our example--further reduces the number of probable crystal structures. The next step is the selection of the probable orientations of the surface layer. Here some energetic considerations are useful: of all the orientations which may be formed those having the lowest values of $\sigma + \sigma_i$ are the most probable. The specific free surface energy σ of the surface layer has its lowest values for equilibrium planes, while the specific free energy σ_i of the interface between surface layer and substrate is lowest for orientations with a small mismatch. The word mismatch is here used not only to mean deviation from a one to one coincidence of the substrate and layer atoms at the interface but also includes deviations from configurations where every nth layer atom coincides with every mth substrate atom (n, m integers).

Once a set of crystal structures and orientations have been chosen the reciprocal lattices of the superimposed structures are constructed by adding all tangential components (with respect to the crystal surface) of the reciprocal lattice vectors of both crystals. Of all the patterns constructed in this way the one which agrees best with the observed pattern is selected. Frequently no complete fit is achieved and lattice distortions in the surface layer up to several percent must be accepted in order to obtain agreement with experiment. This is one of the major limitations

of the pattern interpretation, especially in the case of surface layers with low symmetry where several structures or orientations may be compatible with the diffraction pattern if distortions up to several percent are allowed. We will now illustrate these procedures by some examples.

IV. EXAMPLES OF "SUPERSTRUCTURES"

1. Sixfold Symmetry on Sixfold Symmetry

We consider the simplest case, i.e. identical symmetry--here sixfold two-dimensional symmetry--and orientation. Such a case is observed when Ag is deposited onto a Cu {111} surface (Fig. 3d). Because the deposition was carried out under well defined conditions (well outgassed Ag source, good vacuum and clean Cu surface) there is no doubt that the surface layer consists only of Ag atoms. The {111} plane of Ag has the lowest specific free surface energy and was therefore assumed to be the free surface of the thin layer, i.e. to be parallel to the surface. Figure 3a shows the corresponding reciprocal lattice, Fig. 3b that of the substrate, and Fig. 3c that of the superposition of both crystals. In Fig. 3c only a small number of the reciprocal lattice points are shown, namely those which are near the Cu reciprocal lattice points, as observed in Fig. 3d. This concentration of diffracted intensity in directions near the beams diffracted by the substrate is characteristic for many diffraction patterns of thin surface layers. From the agreement between constructed and observed pattern and from the fact that this pattern is already observed at very low coverage we conclude that Ag grows on the Cu {111} plane in parallel orientation by the monolayer growth mechanism as expected on theoretical grounds.[7] It should be noted that high energy electron diffraction patterns corresponding

to Fig. 3d have been attributed to the dislocation network resulting from the mismatch between the Ag film and the Cu substrate.[8,9] However this interpretation is as unjustified as an interpretation in terms of a true superstructure because the geometrical aspects of the pattern do not allow distinction between mismatch dislocation networks, true and apparent superstructures.

2. Sixfold Symmetry on Fourfold Symmetry -

If Ag is deposited onto a Cu {100} surface under conditions identical to those used in the deposition of Ag onto the Cu {111} plane (see above), the pattern of Fig. 4d is obtained. On the basis of the minimum σ criterion a {111} orientation is to be expected, but it appears possible that a {100} orientation would lead to smaller σ_i. This orientation however can be easily excluded by comparing the theoretically expected pattern with the observed pattern so that, of the two orientations considered, only the {111} orientation remains. With the azimuthal orientation chosen in Fig. 4a with respect to Fig. 4b it gives perfect agreement with experiment as the comparison of Fig. 4c and 4d shows. In Fig. 4c double scattering of the Cu beams with both orientations shown in Fig. 4b (Ag $[11\bar{2}]$ || Cu $[\bar{1}10]$ and Ag $[11\bar{2}]$ || Cu [110]) is taken into account. No lattice distortion is assumed in the construction. Therefore the superstructure spots show characteristic elongations as a consequence of the slight mismatch in the Cu $\langle 110 \rangle$ directions. Some diffraction patterns clearly show the expected elongations indicating that no pseudomorphy occurs. Our result is in apparent disagreement to that of Farnsworth[10] who concluded that Ag films on {100} Cu are amorphous or at least so disordered that they do not

produce a diffraction pattern; a possible reason for this discrepancy is that if parallel growth is expected the orientation observed by us can be easily missed in a scanning type system when observations are made only in selected azimuths. The orientation reported here fits reasonably well into the mutual orientation scheme for f.c.c. metals given by Shirai et al.[11]

Recently Tucker[12] reported complex LEED patterns obtained from a Rh {100} surface after heating in oxygen. He attributed these to a misfitting monolayer of oxygen atoms or ions. Quadrants of the patterns are shown schematically in Fig. 5a, b, after elimination of the distortion produced by the deflection field. The patterns are very similar to Fig. 4c and suggest an interpretation in terms of a Rh-oxide surface layer. If Fig. 5a, b are interpreted in the same manner as Fig. 4c, i.e. by a thin surface layer with cubic structure, with its {111} plane parallel to the surface and its $[11\bar{2}]$ direction parallel to Cu $[1\bar{1}0]$ and [110], then this layer must have a lattice constant a = 4.40 Å. Another interpretation would be in terms of a layer with hexagonal structure with its (001) plane parallel to the substrate and a = 6.21 Å. Of the reported oxides (Rh_2O_3, RhO, Rh_2O),[13] only the structure of Rh_2O_3 is known: It is hexagonal with a = 5.11 Å, which is clearly incompatible with the diffraction pattern. Although it has been shown recently that only Rh_2O_3 exists in the bulk,[14] the existence of RhO and/or Rh_2O as a surface phase appears reasonable. A probable structure for Rh_2O is--by analogy with Cu_2O, Ag_2O and Pb_2O--the cuprite structure. If we assume a linear relation between the lattice constants of the metals and their oxides, then a_{Rh_2O} = 4.43 Å in reasonable

agreement with the value a = 4.40 Å deduced from the pattern. By analogy with Cu_2O, the {111} plane of Rh_2O is expected to be an equilibrium plane and therefore parallel to the surface. This agreement between experiment and the expectations for a Rh_2O layer, together with the unfavorable energetics of Tucker's densely packed oxygen layer, makes the present interpretation much more likely than the one originally proposed .

Another example for a superposition of sixfold symmetry and fourfold symmetry is the (5x1) structure found on Au {100} and Pt {100} planes.[15-18] As shown elsewhere in more detail, it can be attributed in the case of Au to a thin layer of Au_2Na or Au_2K with (111) Au_2Na || (001) Au, $[11\bar{2}]$ Au_2Na || $[1\bar{1}0]$ and [110] Au. It appears very likely that the same interpretation applies to the Pt (5x1) structure.

3. Sixfold Symmetry on Twofold Symmetry

One of the most complex LEED patterns reported to date[4,19] is that of carbon on the W {110} plane. It was originally attributed to a dilute compound superstructure with composition $W_{15n}C$ with n = 2 or 4.[19] We have obtained this structure under conditions (heating in CH_4) which are known to lead to W_2C formation on tungsten. Consequently only W_2C was considered in the interpretation of the pattern. Fig. 6d shows the LEED pattern from a specimen region in which only one of the two equivalent orientations is formed. This pattern is not compatible with the orientation relationship derived from X-ray studies of carburized wires.[20] We have examined the following orientations: (100), (010) and (001) α-W_2C || (110) W and (111) β-W_2C ‖ (110) W which is equivalent to (001) α-W_2C ‖ (110) W--as long as only geometrical aspects of the patterns are considered--because

$a_{\beta\text{-}W_2C} = 4.26$ Å $\simeq \sqrt{2} \cdot 2.99$ Å $= \sqrt{2}\, a_{\alpha\text{-}W_2C}$,[21] which is the condition for the identity of the corresponding reciprocal lattice. The orientation relationship which agrees best with Fig. 6d is shown in Fig. 6a and b; Fig. 6c shows the reciprocal lattice of the superimposed crystals. The orientation relationship, referred to the cubic modification is (111) β-W_2C || (110) W, [1$\bar{1}$0] β-W_2C || [$\bar{1}$15] W, or referred to the hexagonal modification (001) α-W_2C || (110) W, [100] α-W_2C || [$\bar{1}$15] W. This orientation relationship leads to a nearly perfect coincidence of the atoms with the following coordinates in the contact planes (N, M being integers):

atoms in W (110) plane:	(000)	N (11$\bar{2}$)	M $\left(\frac{\bar{5}}{2}\ \frac{5}{2}\ \frac{5}{2}\right)$
atoms in α-W_2C (001) plane:	(000)	N ($\bar{3}\bar{2}$0)	M (1$\bar{4}$0)
atoms in β-W_2C (111) plane:	(000)	N $\left(\frac{1}{2}\ \frac{\bar{3}}{2}\ 1\right)$	M $\left(\frac{\bar{5}}{2}\ \frac{1}{2}\ 2\right)$

It should be noted that the "superstructure" pattern of Fig. 6d is not the only one observed in the system C-W {110}. We have frequently observed a pattern which has the same periodicity in the [1$\bar{1}$1] direction as Fig. 6d, but a four times larger periodicity in the [1$\bar{1}\bar{2}$] direction. No effort has been made to index this pattern.

4. Twofold Symmetry on Twofold Symmetry

The final example is intended mainly to demonstrate the difficulties which are encountered when the composition of the surface layer is not known reliably, when the crystal structure of the suspected compound has a low symmetry, when the anisotropy of its surface energy is not known, and when no orientation fits the diffraction nearly perfectly. Such a pattern is that obtained on a W {110} surface when exposed while heated above 700°C to sufficient oxygen so that more than 1/2 monolayer of oxygen

reacts with the crystal. This pattern, first reported by Germer and May[22] as C(48 x 16) structure without further interpretation, is shown in Fig. 7d. On the basis of its formation conditions we attribute it to WO_2. WO_2 has a pseudotetragonal orthorhombic structure with a_o = 5.65 Å, b_o = 4.89 Å, c_o = 5.55 Å, β = 120.4°,[23] which deviates so little from the tetragonal symmetry with a_t = 4.86 Å ($\equiv b_o$), c_t = 2.77 Å ($\equiv |\underset{\sim}{b}_o - \underset{\sim}{c}_o|$) that the projections of the reciprocal lattices of both structures practically coincide. We have examined the following orientations: $(100)_o$, $(010)_o$, $(001)_o$, $\{100\}_t$, and $(001)_t$ WO_2 || (110) W with the result that no orientation gave a nearly perfect fit to the observed pattern unless lattice distortions were assumed, but that several orientations were compatible with the pattern if lattice distortions of up to 6% in the axis lengths and up to 5° in the angle between the axes were permitted and if it was assumed in some cases that certain reciprocal lattice rods expected from the symmetry of the bulk crystal were missing. The two most probable orientations arrived at are $(010)_o$ WO_2 || (110) W, $[001]_o$ WO_2 = || $[1\bar{1}0]$ W and $(100)_t$ WO_2 || (110) W, $[012]_t$ WO_2 || $[3\bar{3}\bar{2}]$ W. The second orientation relationship and the resulting reciprocal lattice is shown in Fig. 7a-c. Distortions of 3.9% and 0% in the b and c directions respectively and of 1° in α had to be assumed. The same interpretation can be given to the diffraction pattern reported by Germer and May[22] as C(21 x 7) structure, which is formed at higher oxygen doses or upon heating the crystal showing the pattern of Fig. 7d at room temperature above 700°C. According to our measurements it has the same periodicity along the rows of spots and differs from the pattern of Fig. 7d mainly by the concentration of the spot intensities in the environment of the tungsten

spots. A discussion of the differences between the two patterns will be given elsewhere.

DISCUSSION

We have illustrated with some examples how "superstructure" patterns can be interpreted in terms of double scattering between structures well known from bulk crystal structure analysis, involving only minor lattice distortions of the surface layers. As pointed out previously an analysis of the geometrical aspects of the diffraction pattern does not allow distinction between different structures which give rise to the same two-dimensional "superstructure" periodicity, such as true superstructures, misfit dislocation networks, and apparent superstructures formed by two-dimensional coincidence lattices or as discussed here by structures known from the bulk. As long as no reliable theory is available to interpret the spot intensities in terms of the distribution of the atoms within the "superstructure" unit cell the choice between the various possibilities has to be made on the basis of the formation conditions of the structure, stability considerations, surface potential measurements, etc. On the basis of such considerations we believe that the interpretations based on known structures which we have given here are more probably correct than those suggested previously for the same patterns. We suggest that all "superstructure" patterns be analyzed in this way before they are ascribed to exotic two-dimensional surface structures.

ACKNOWLEDGMENT

The author wishes to thank Dr. J. O. Porteus for critically reading the manuscript.

REFERENCES

1. E. Bauer, Phys. Rev. 123, 1206 (1961).
2. C. W. Tucker, Jr., Appl. Phys. Letters 3, 98 (1963).
3. C. W. Tucker, Jr., J. Appl. Phys. 35, 1897 (1964); Surface Sci. 2, 516 (1964).
4. E. Bauer, Colloqu. Intern. CNRS 1965, No. 152, p. 19.
5. N. Taylor, Surface Sci. 4, 161 (1966).
6. J. J. Lander, Surface Sci. 1, 125 (1964).
7. E. Bauer, Z. Kristallogr. 110, 372 (1958).
8. U. Gradmann, Phys. Kondens. Materie 3, 91-98 (1964).
9. G. O. Krause, J. Appl. Phys. 37, 3694 (1966).
10. H. E. Farnsworth, Phys. Rev. 49, 605 (1936).
11. S. Shirai and Y. Fukuda, J. Phys. Soc. Japan 17, Suppl. B-II, 319 (1962).
12. C. W. Tucker, Jr., J. Appl. Phys. 37, 3013 (1966).
13. L. Wöhler and W. Müller, Z. Anorg. Chem. 149, 135 (1925).
14. N. G. Schmahl and E. Minzl, Z. physik. Chem. 41, 78 (1964).
15. S. Hagstrom, H. B. Lyon, and G. A. Somorjai, Phys. Rev. Letters 15, 491 (1965).
16. D. G. Fedak and N. A. Gjostein, Phys. Rev. Letters 16, 171 (1966).
17. E. Bauer, unpublished results.
18. E. Bauer, A. K. Green, and K. M. Kunz, Appl. Phys. Letters 8, 248 (1966).
19. R. M. Stern, Appl. Phys. Letters 5, 218 (1964).
20. R. A. Swalin, Acta Cryst. 10, 473 (1957).
21. H. J. Goldschmidt and J. A. Brand, J. Less-Common Metals 5, 181 (1963).
22. L. H. Germer and J. W. May, Surface Sci. 4, 452 (1966).
23. A. Magneli, G. Anderson, B. Blomberg, and L. Kihlborg, Anal. Chem. 24, 1998 (1952).

FIGURE CAPTIONS

Fig. 1. Schematic surface layer structures: (a) true superstructure (with sixfold periodicity of substrate crystal, c = 6a); (b) apparent superstructure (misfitting layer, 5b = 6a).

Fig. 2. Reciprocal lattice sections: (a) superposition of reciprocal lattices of two different structures; (b) reciprocal lattice of the superposition of two different structures (5b = 6a).

Fig. 3. Diffraction by sixfold symmetry on sixfold symmetry (Ag on Cu {111} plane). (a), (b), and (c) reciprocal lattice of Cu, Ag and superposition of Ag and Cu respectively; (d) diffraction pattern taken at 60 V.

Fig. 4. Sixfold symmetry on fourfold symmetry (Ag on Cu {100} plane). (a), (b), and (c) reciprocal lattice of Cu, Ag and superposition of Ag and Cu respectively; (d) diffraction pattern taken at 90 V. (d) Should be rotated 45° to agree with the (a) - (c). The squares and large full circles are due to the two orientations of the Ag layer, the small full circles are secondary scattering spots.

Fig. 5. Schematic diffraction pattern obtained from Rh {100} surface after heating in oxygen at 400°C according to Tucker,[12] interpreted in terms of epitaxial Rh_2O. Open circles Rh, large full circles Rh_2O in orientation I, full squares Rh_2O in orientation II, small full circles secondary scattering spots.

Fig. 6. Sixfold symmetry on twofold symmetry (W_2C on W {110} plane). (a), (b), and (c) reciprocal lattice of W, W_2C, and superposition of W_2C and W respectively; (d) diffraction pattern taken at 210 V.

Fig. 7. Twofold symmetry on twofold symmetry (WO_2 on W {110} plane). (a), (b), and (c) reciprocal lattice of W, WO_2 and superposition of WO_2 and W respectively; (d) diffraction pattern taken at 80 V.

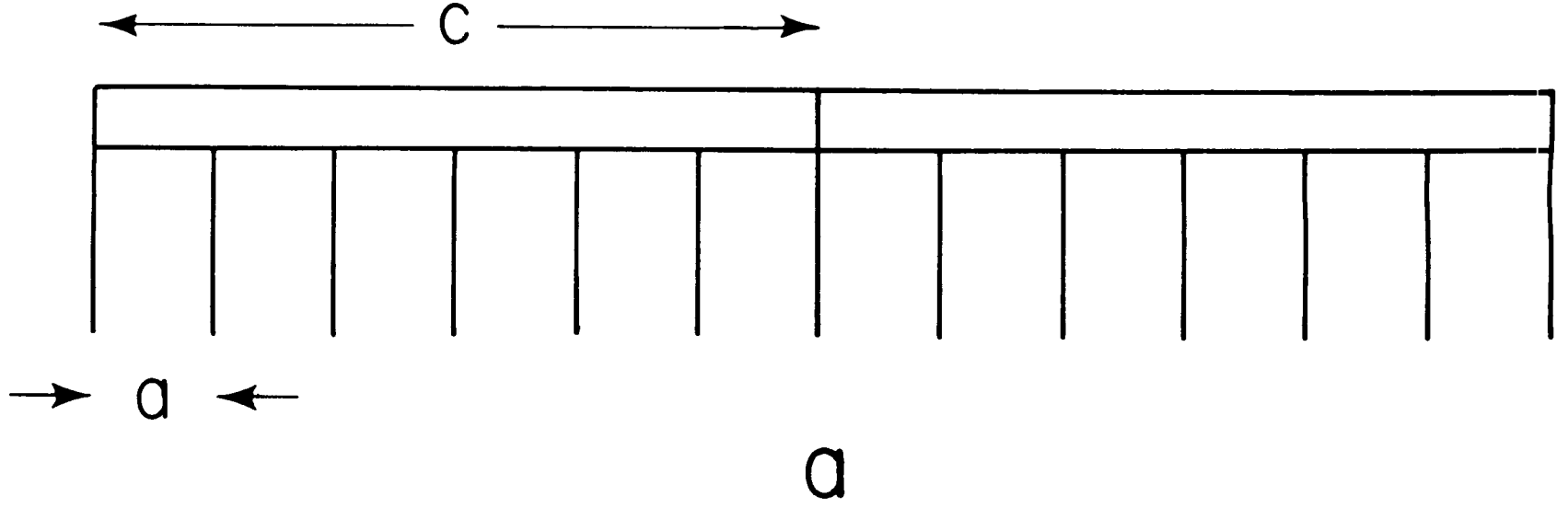

a

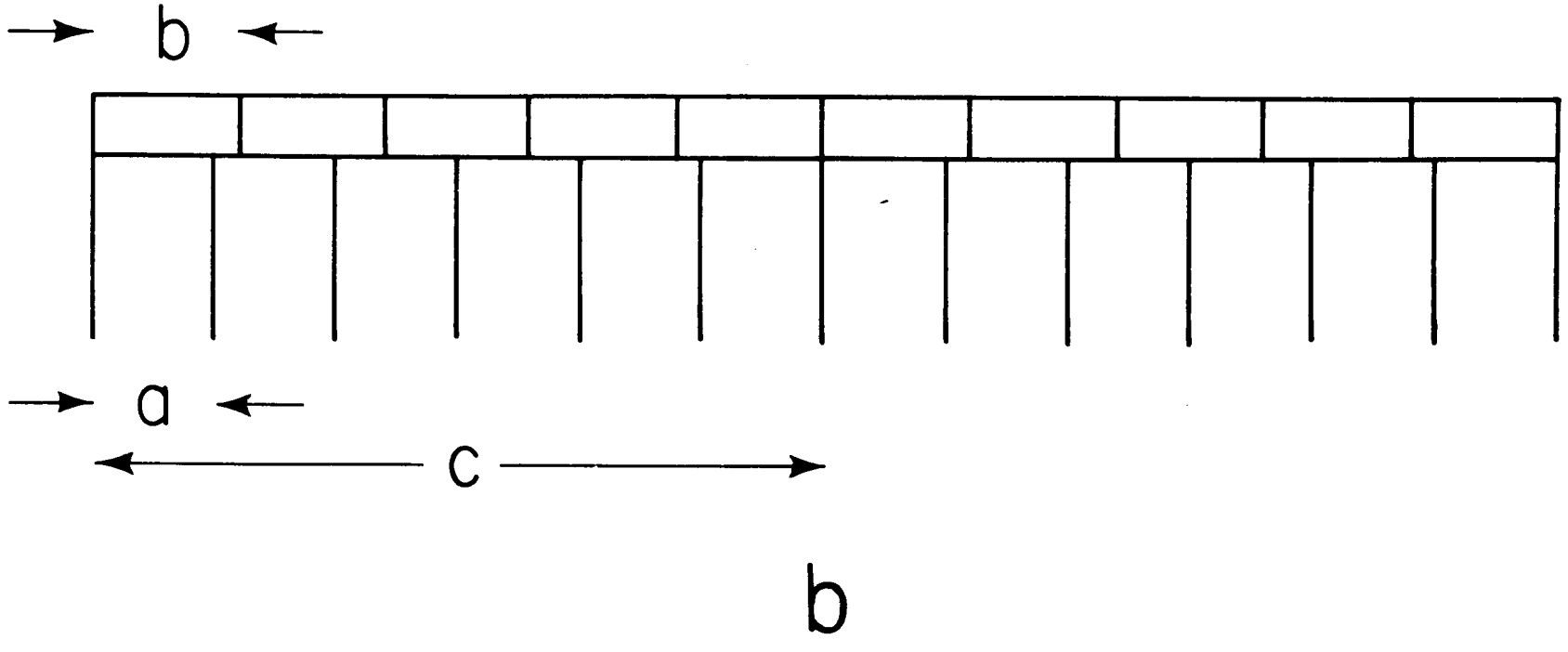

b

FIG. 1

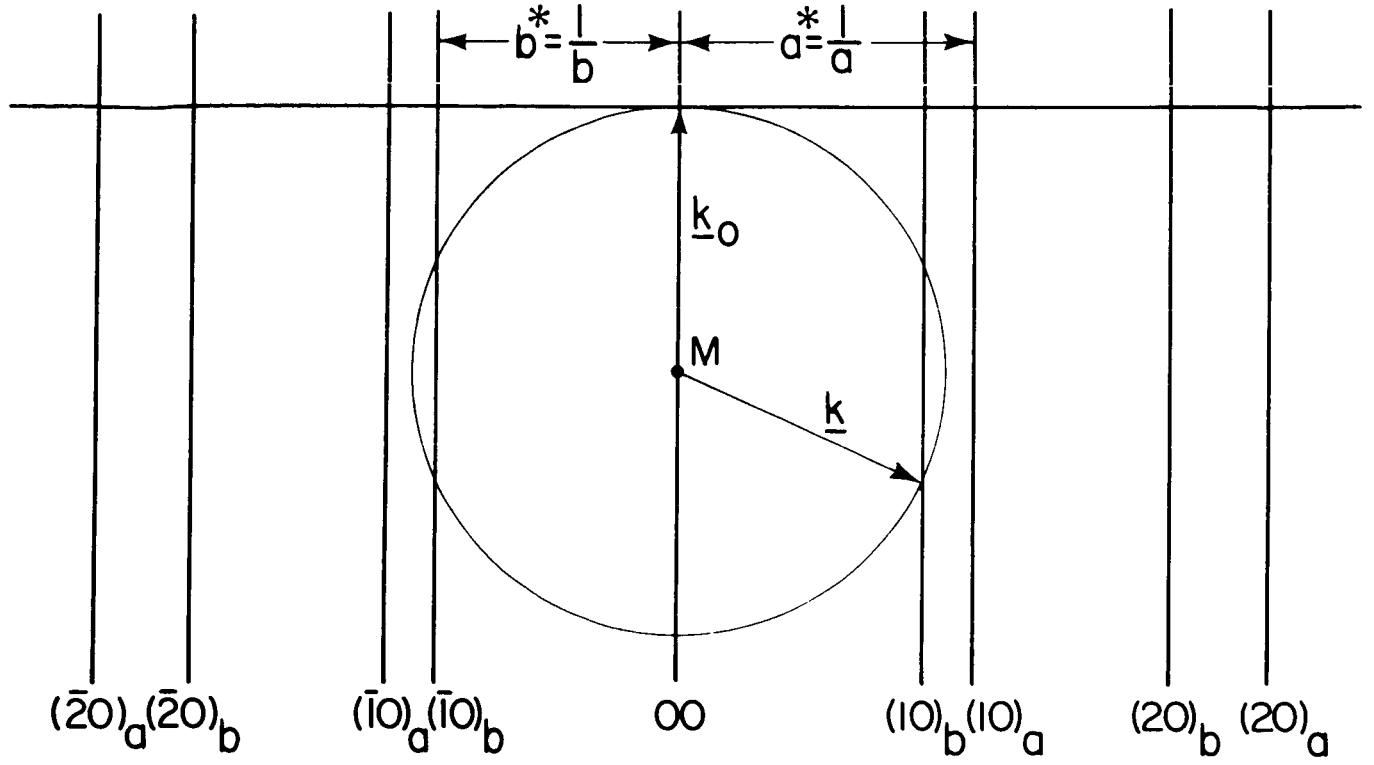
$b^* = \frac{1}{b}$
$a^* = \frac{1}{a}$
$\underline{k}_o$
M
$\underline{k}$
$(\bar{2}0)_a(\bar{2}0)_b$
$(\bar{1}0)_a(\bar{1}0)_b$
00
$(10)_b(10)_a$
$(20)_b$ $(20)_a$

a

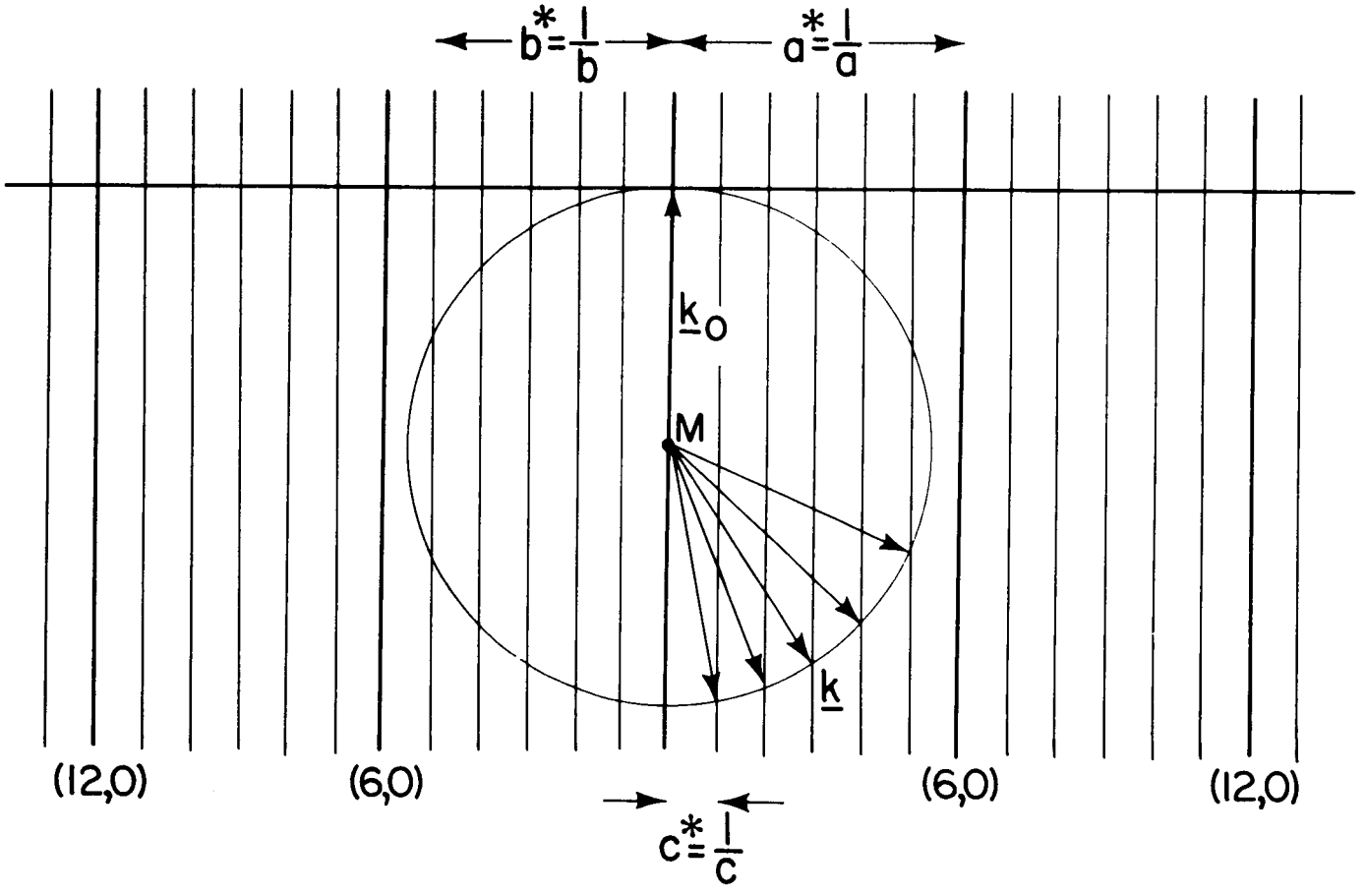
$b^* = \frac{1}{b}$
$a^* = \frac{1}{a}$
$\underline{k}_o$
M
$\underline{k}$
(12,0)
(6,0)
(6,0)
(12,0)
$c^* = \frac{1}{c}$

b

FIG. 2

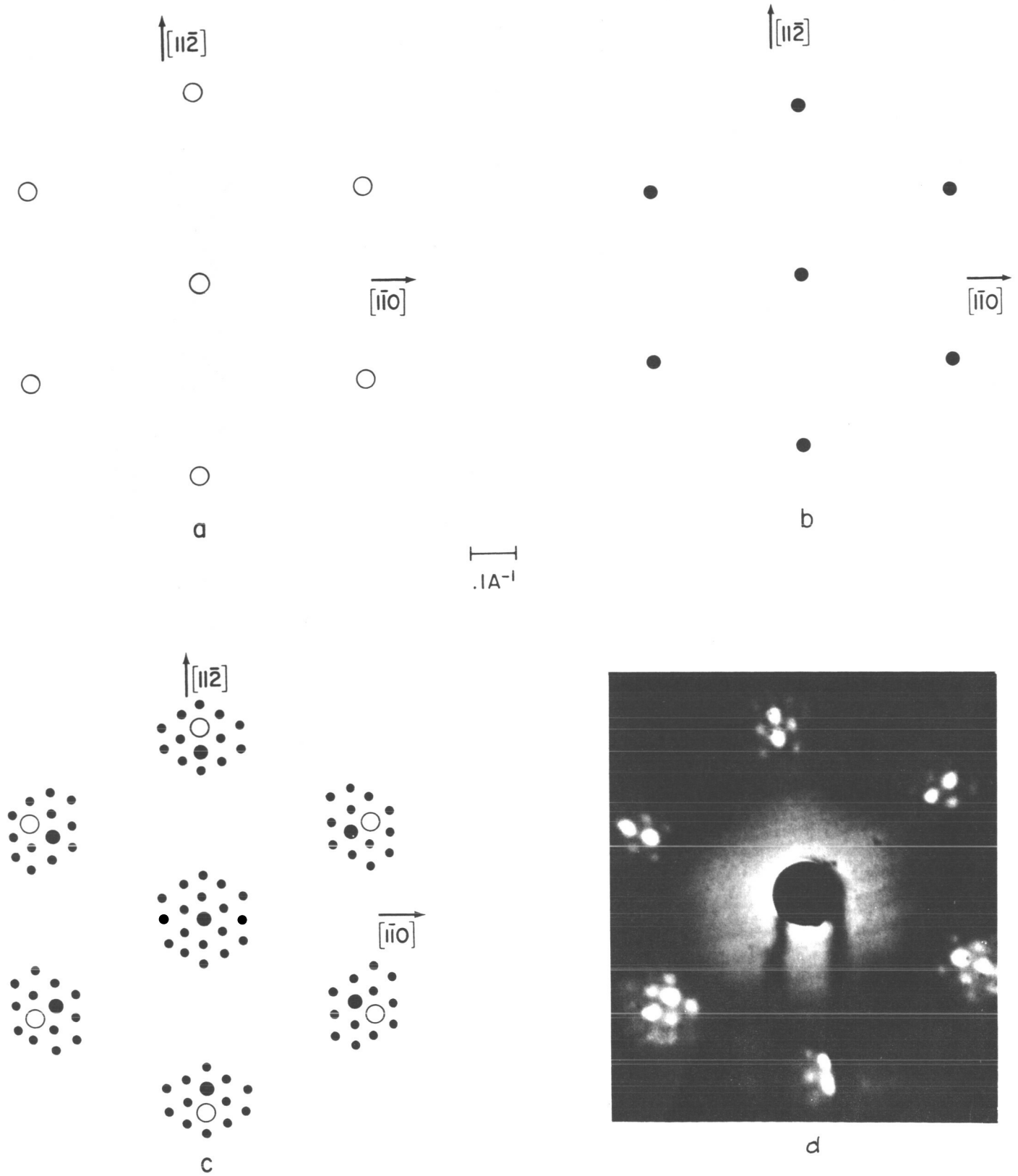

FIG. 3

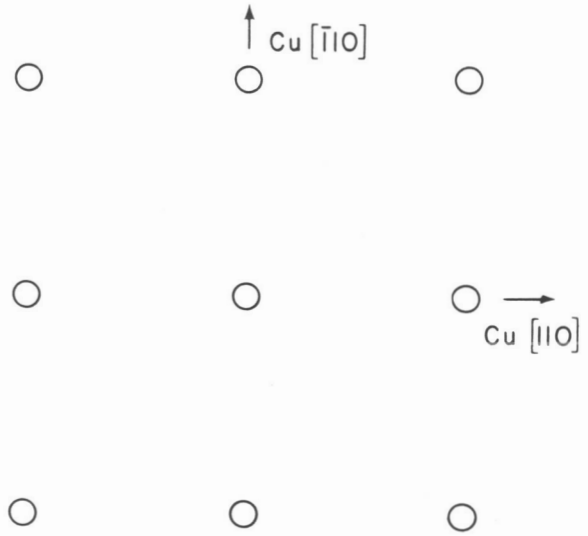

a

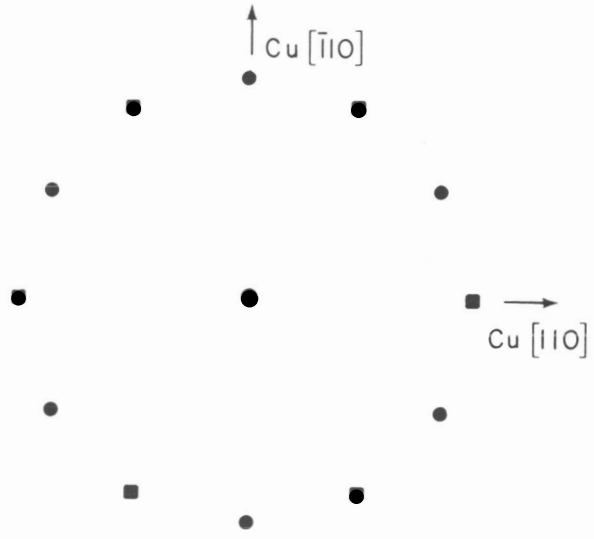

b

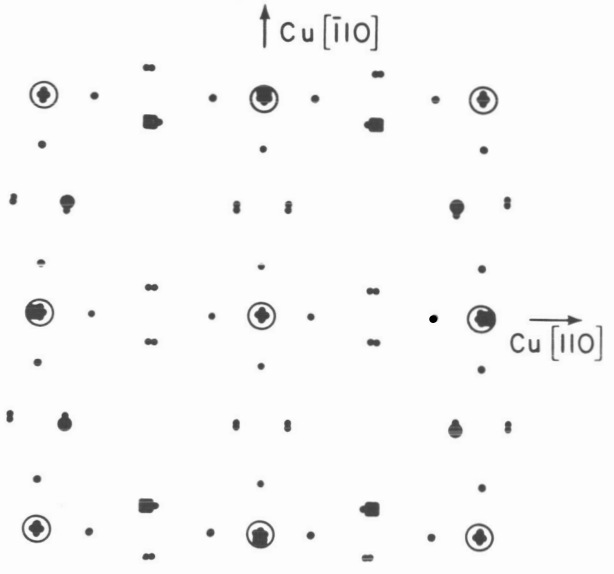

c

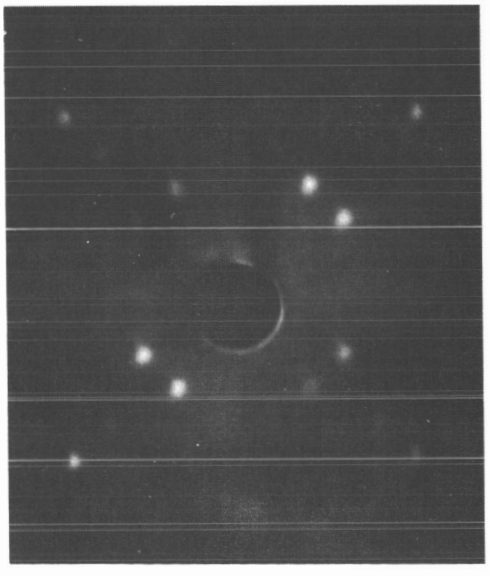

d

FIG. 4

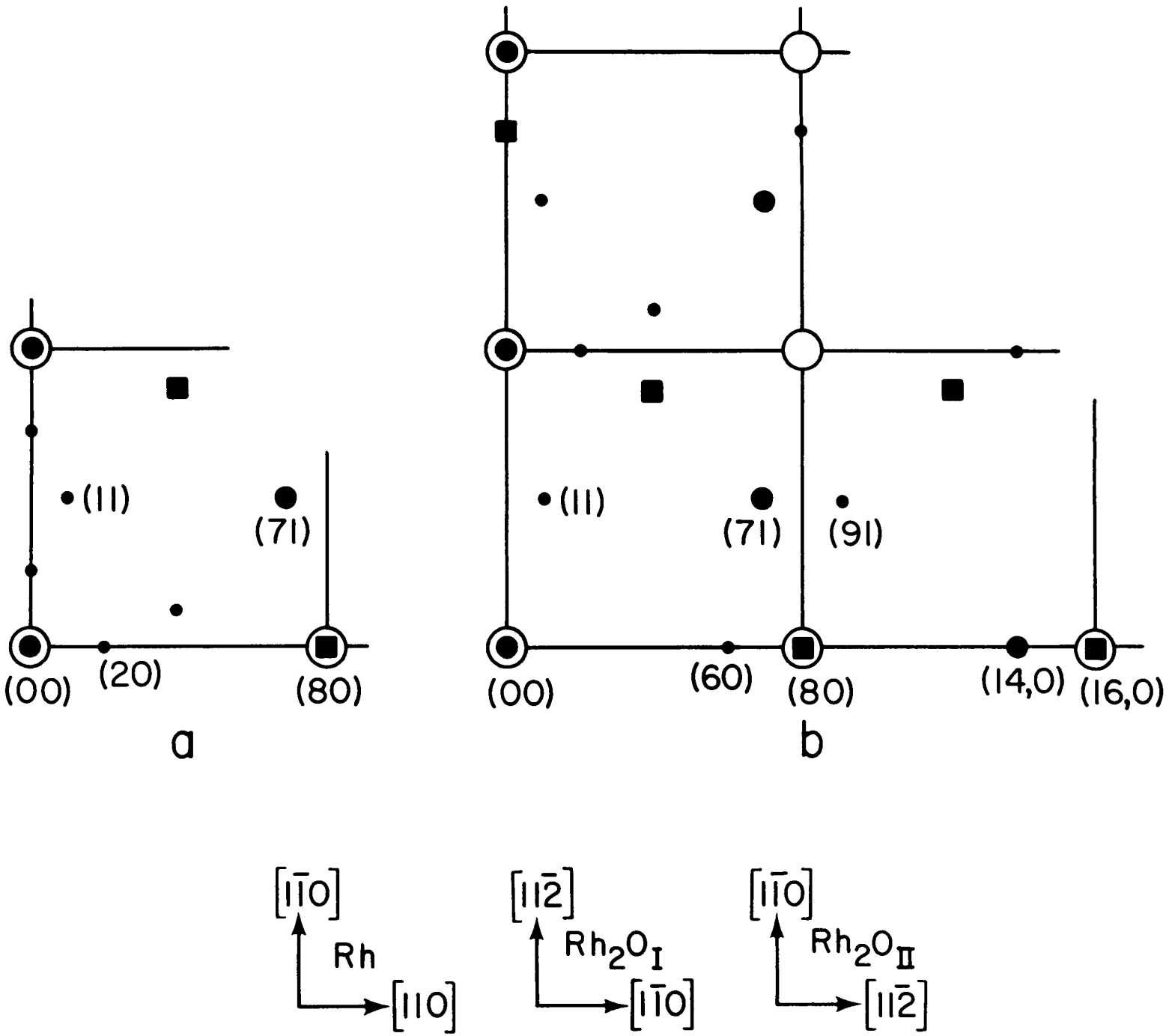
(11)
(71)
(00)
(20)
(80)
a
(11)
(71)
(91)
(00)
(60)
(80)
(14,0)
(16,0)
b
[1$\bar{1}$0]
Rh
[110]
[11$\bar{2}$]
Rh_2O_I
[1$\bar{1}$0]
[1$\bar{1}$0]
Rh_2O_{II}
[11$\bar{2}$]

FIG. 5

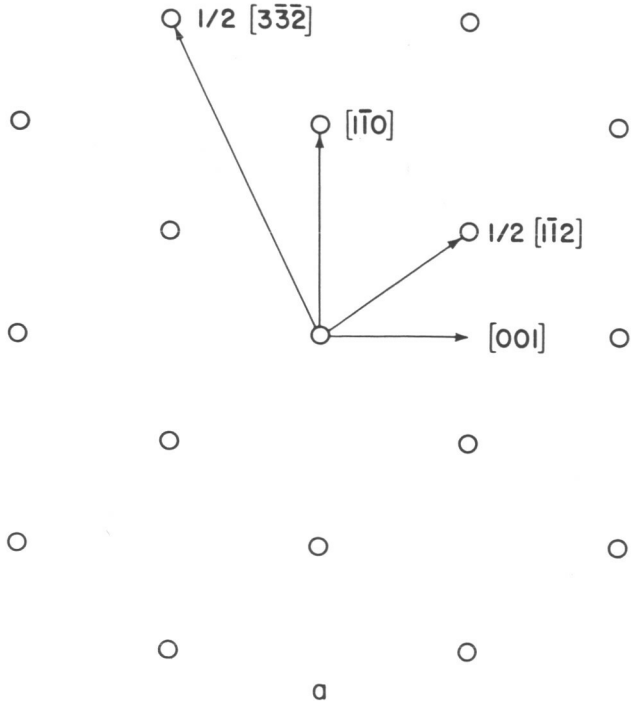

a

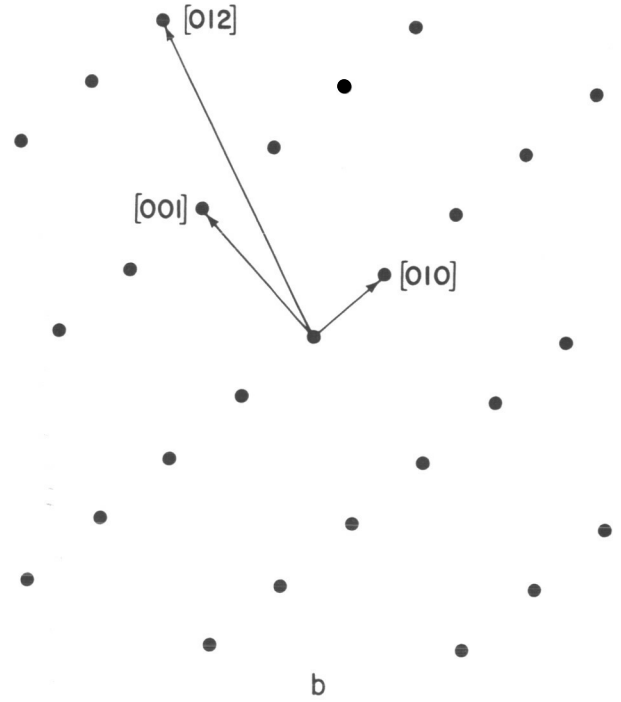

b

.1A^{-1}

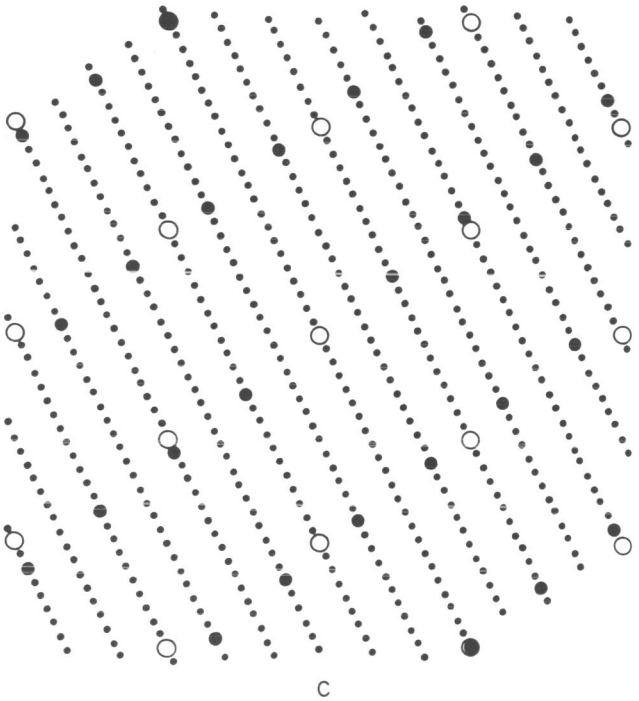

c

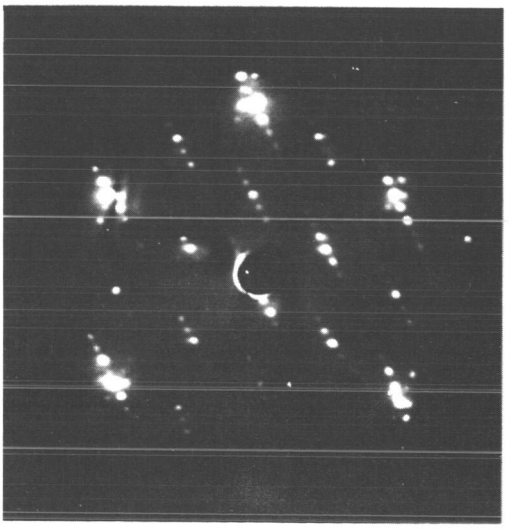

d

FIG. 7

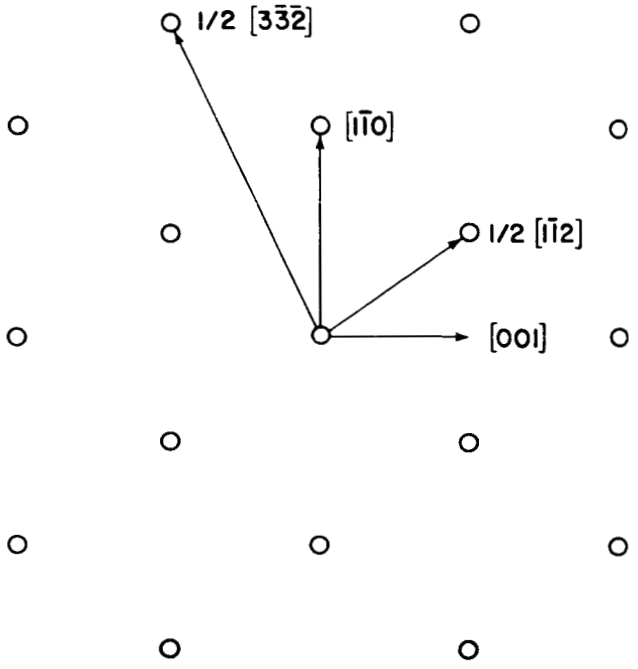

a

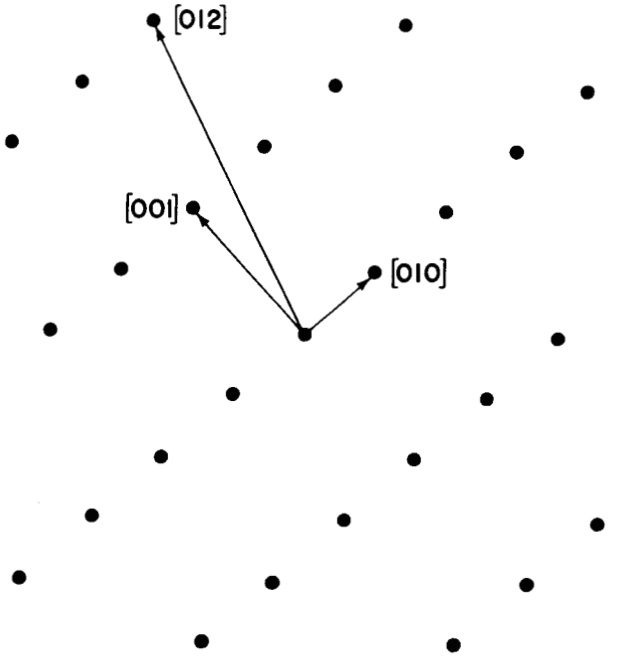

b

.1A^{-1}

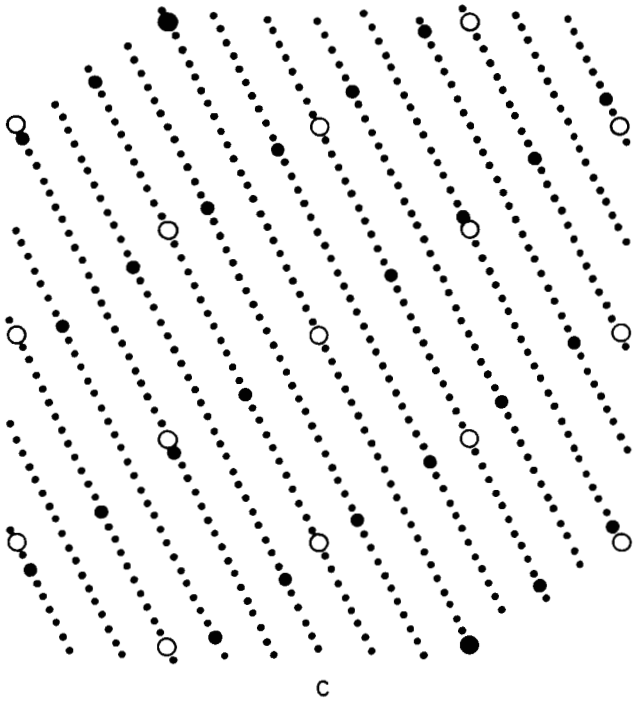

c

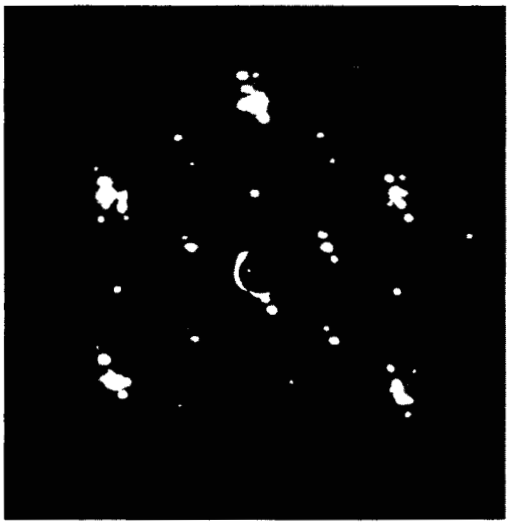

d

FIG. 7

Linear Unfolding Methods and Optimization for X-Ray and Similar Spectra

J. O. Porteus

U. S. Naval Ordnance Test Station, China Lake, California

ABSTRACT

The problem of correcting x-ray spectra and similar data for linear smearing or resolution loss, i.e., unfolding, is reexamined with emphasis on accuracy limitations. The advantage of optimum smoothing or filtering in minimizing the effects of experimental uncertainties is demonstrated by comparing three methods when applied to a simple example. The related roles of nonstationarity and the sample span in optimization are considered in detail with reference to such common difficulties as flattening of line peaks, excessive noise in line tails and spurious oscillations near large changes in spectral intensity. Refinements tending to alleviate these difficulties are discussed, along with ultimate limitations. Also discussed is a means of sampling integrated spectra, which is useful when the unfolding includes a differentiation, as in processing electron energy-loss spectra measured with a retarding field.

Linear Unfolding Methods and Optimization for X-Ray and Similar Spectra

J. O. Porteus

U. S. Naval Ordnance Test Station, China Lake, California

INTRODUCTION

The subject of unfolding or making resolution corrections to experimental data has received considerable attention in the literature, especially in the field of x-ray physics.[1-3] Although many useful methods have been proposed, relatively little attention has been given to optimization and ultimate accuracy limitations. Although such considerations may be of questionable practical importance when unfolding corrections are small, the amplification of experimental uncertainties which accompanies the large corrections often required in x-ray spectra demands the best accuracy reasonably obtainable. An optimized method (OPT) designed for such critical situations has been reported by the author.[1] The first aim of the present paper is to demonstrate the importance of optimization on the basis of comparative accuracy considerations, including both variance and expectation

value of solutions. The benefits of optimization can be fully realized only when proper allowance is made for the nonstationary character of x-ray spectra and for the restrictions on sample span thus imposed. A second aim of the paper is therefore to analyze the roles of nonstationarity and sample span with possible improvement of OPT as an objective. A third aim is to develop a means of sampling for integrated spectra, which is useful in application of OPT to the unfolding of electron energy loss data measured by the retarding field method.[4]

Basically, all unfolding methods provide solutions, with varying degrees of generality, of the folding or convolution integral equation

$$O(\nu) = \int_{-\infty}^{\infty} [M(\nu,\nu-\nu') - E_M(\nu,\nu-\nu')]\, T(\nu')d\nu' + E_O(\nu). \qquad (1)$$

In the x-ray case O is an observed or measured spectrum, a function of x-ray spectral frequency ν; T is the true or desired spectrum; M may represent the instrumental window or any other smearing function which linearly limits the resolution of T. The terms E_M and E_O in the integral equation represent the uncertainties or noise arising from statistical experimental inaccuracies in M and O, respectively.

If the exact $M\text{-}E_M$ is given and depends effectively only on $\nu-\nu'$ within the ν-interval involved in the unfolding of any given spectral point, and if M is such that T is uniquely determined by $O\text{-}E_O$, Eq. (1) may be solved formally, giving

$$T(\nu) \cong \int_{-\infty}^{\infty} V(\nu,\nu-\nu') \left[O(\nu')-E_O(\nu')\right]d\nu', \qquad (2)$$

where the approximation involves only the explicit ν-dependence of M, as shown in the appendix. Although Eq. (2) may appear in different forms, the operator concept is applicable to all unfolding methods. Moreover the operators V associated with all unfolding methods are equivalent in principle in the sense that all produce the same true spectrum when applied strictly to $O-E_O$, i.e., to O in the limit of vanishing noise. In this context it would appear that the most desirable unfolding method is the one involving minimum labor in computing V and applying Eq. (2) or its equivalent. In practice, however, this is not necessarily the case since V must be applied to O rather than to $O-E_O$. When the E_O term is included the equivalence of different unfolding operators vanishes and the question of the optimum operator arises.

Further complexity is introduced when M contains an uncertainty E_M, which may also influence the optimization of V. Such optimization with respect to E_M assumes maximum importance when detailed knowledge of the smearing function is poor, so that a solution with minimum sensitivity to error within the limited specification of M becomes essential. In the examples given here E_M is generally excluded in order to avoid nonessential complications in discussing the E_O term, which is more significant in most practical situations. However, E_M is included in the general discussion and the principles illustrated by the examples remain valid.

COMPARISON OF METHODS

The effect of optimization is best demonstrated by comparing OPT with non-optimum methods in solving a hypothetical unfolding problem where the solution is known, as in Figs. 1 and 2. As shown schematically in the inset of Fig. 1, the true spectrum is taken to be a Lorentzian of half-width β at half-maximum, and the observed spectrum is a Lorentzian of twice this width. The smearing function, which happens to be identical to the true spectrum in this example, is assumed given. Unless otherwise stated, the observed spectrum is hypothetically measured at intervals of 0.2β with an uncorrelated rms error amounting to 1% of the observed peak intensity over the entire spectral region. This corresponds to the input noise level indicated by the vertical bar at the bottom left of these figures. Corresponding output noise levels of the various solutions, as computed from a variance analysis, are similarly indicated along the unfolded curves. Figure 1 compares a method of iterated convolutions (IC), apparently originated by van Cittert,[5] with OPT. In IC the V is a sum of terms, each consisting of multiple convolutions of M with itself. The highest multiplicity of convolutions appearing corresponds to the order of approximation, which number accompanies each of the IC solutions given in the figure. Termination of the sum after a finite number of terms is equivalent to the introduction of a one-parameter linear mathematical filter, similar to that used by OPT.

Such a filter is characterized by a smoothing function, actually a special type of smearing function, applied to the observed spectrum in the unfolding process. The filter parameter, which determines the amount of smoothing or filtering in both methods, is the appropriate order of approximation in IC, while in OPT it is essentially the signal-to-noise ratio averaged over a finite range of ν. The most significant difference between the two methods is the greater inherent efficiency of the filter in the OPT case. At the peak of the Lorentzian, for example, the expectation value of the IC solution deviates from the true spectrum by more than the OPT curve through the eleventh order, while the noise level exceeds that of OPT after only the second order.

Figure 2 compares the derivative method (D) of Sachenko[6] with the OPT method. Derivatives are evaluated by a finite central difference calculation, which produces a weighted average over a number of data intervals, the actual number being dependent on the highest order difference included. This again leads to a linear operator formulation with the maximum included order of difference acting as the parameter of a linear mathematical filter. The zeroth order D solution is in fact identical with the first order IC solution, but the termwise convergence of the former is more rapid in the higher orders. As with OPT, proper filtering in D of each data point is determined from calculations on a local sample of the observed spectrum, i.e., from the calculated central

differences, whose magnitudes are compared with noise levels in the corresponding solutions. Since no independent interpolation procedure is used in D, filtering in this case depends to a considerable degree on the size of the data interval. The D curve in Fig. 2 was prepared on the basis of a data interval of 0.7β, which (at the Lorentzian peak) is the largest compatible with Sachenko's eighth order difference limitation.[6] Although for the most part this produces a better solution than smaller intervals, the noise level is generally excessive compared to OPT, as shown in the figure. The expectation value of D on the other hand, except for irregularities produced by the required changes in order of approximation along the curve, compares reasonably well with the OPT curve.

These examples demonstrate the difficulty of achieving both small variance and accurate expectation, which always tend to be incompatible in unfolding. Optimum choice of the effective filter parameters in any given method can achieve a balance between these two divergent aims, but only optimum design of the filter itself can insure the best possibility of achieving these aims simultaneously.

While the advantage of the OPT solution is clear in these comparisons, some deficiencies are also apparent. At the Lorentzian peak, for example, the deviation of the OPT curve from the true curve is substantially in excess of the noise level; while in the tail region beyond about 4β the

reverse is true. Also, spurious oscillations tend to appear. The source of these problems lies largely in the inability of the filter parameter to respond sufficiently to large localized changes in the signal-to-noise ratio. This effect, which is associated with the nonstationarity of the observed spectrum, occurs quite generally in unfolding. In both IC and D, for example, the effect is apparent in the fact that a higher order of approximation is required near the Lorentzian peak than in the tail region. From the computational standpoint nonstationarity always presents a difficult problem since it introduces into V an explicit ν-dependence which usually is much more pronounced than that associated with M. In the present work, however, attention will be restricted to the theoretical aspect of the problem and to the possibility in principle of reducing the residual deficiencies in OPT resulting from nonstationarity.

THEORY

Before proceeding further it is necessary to review carefully the origin of the stationarity approximation and its limitations. The optimization problem in unfolding is equivalent in many respects to that of optimum signal extraction in communication theory. Various formulations are possible, the most comprehensive being in terms of statistical decision theory.[7] Figure 3 illustrates the unfolding problem schematically from this point of view. Since T and

$L \equiv M-E_M$ are independent and never known exactly, they may be regarded as members of statistical ensembles which occupy the function spaces Ω_T and Ω_L, respectively. These spaces combine with each other through the convolution operation (*) and then additively (+) with a third space occupied by the noise E_O to form the space Γ_O associated with the observed spectrum O. The measured or observed smearing function M, which is also subject to statistical fluctuations, occupies the space Γ_M generated by the additive combination of Ω_L space with the space occupied by the noise E_M. The box represents a decision rule δ into which are fed O and M and out of which come decisions concerning the true spectrum, which occupy the decision space Δ. The decisions of interest here, of course, are actual estimates $\mathcal{T}$ of T.

Optimized unfolding amounts to finding optimum decision rules, which first requires some means for evaluating such rules. This is accomplished by choosing, somewhat arbitrarily, a certain cost function and evaluation function. The cost function, which is actually a functional of T and $\mathcal{T}$, assigns a certain cost or loss to each combination of input T and decision $\mathcal{T}$. An example is the quadratic cost function

$$C(T,\mathcal{T}) = |T - \mathcal{T}|^2, \qquad (3)$$

which is used by OPT. Since statistical quantities are involved, a means of averaging must be provided in order to arrive at the actual loss rating for each decision rule. This is the purpose of the evaluation function, an example being the expectation or average value of the cost function, which

is the form normally chosen. The average loss rating thus formulated in terms of the distribution densities, which are functionals characterizing the statistics of the various spaces of Fig. 3, takes the form of an average risk

$$R(\tau,\lambda,\delta) = \langle C(T,\mathfrak{T}) \rangle =$$

$$\int_{\Omega_T}\int_{\Omega_L}\int_{\Omega_O}\int_{\Omega_M} C(T,\mathfrak{T})\tau(T)\lambda(L)W_O(O-L*T) \times W_M(M-L)\,dT\,dL\,dO\,dM, \tag{4}$$

where non-randomized decision rules have been excluded. That is, each given combination of O and M are allowed to produce only one $\mathfrak{T}$ with unity probability, so that $\delta(\mathfrak{T}|O,M)$ becomes a delta function and integration over Δ space is trivial.[8] With this restriction minimization of R with respect to $\mathfrak{T}$ leads to the so-called Bayes estimator for T

$$\mathfrak{T}^B_{\tau\lambda}(O,M) = \frac{\int_{\Omega_T}\int_{\Omega_L} T\tau(T)\lambda(L)W_O(O-L*T)W_M(M-L)\,dT\,dL}{\int_{\Omega_T}\int_{\Omega_L} \tau(T)\lambda(L)W_O(O-L*T)W_M(M-L)\,dT\,dL}. \tag{5}$$

A difficulty with Bayes estimation, although not the most serious one, is that $\mathfrak{T}^B$ generally represents a nonlinear operation on the observed spectrum. The problem is simplified considerably if the estimators are restricted to the class of linear operators. One then seeks the estimator which minimizes the average risk within this smaller class. Introducing the linear operator V such that $\mathfrak{T} = V*O$, the

quadratic cost function of Eq. (3) becomes equal to E_t^2 of OPT. If $L(\nu,\nu-\nu')$ is approximated by $L(\nu_0,\nu-\nu')$, the average risk of linear estimators R^l may be written explicitly,

$$R^l(\tau,\lambda,\delta) \cong \langle E_t^2[\nu_0,O(\nu),T(\nu)]\rangle$$

$$= \int_{-\infty}^{\infty}\int_{-\infty}^{\infty} \{\langle [\hat{V}(z)\hat{L}(\nu_0,z)-1][\hat{V}^c(z')\hat{L}^c(\nu_0,z')-1]\rangle \times$$

$$\langle \hat{T}(z)\hat{T}^c(z')\rangle + \hat{V}(z)\hat{V}^c(z')\langle \hat{E}_0(z)\hat{E}_0^c(z')\rangle\} \times$$

$$e^{2\pi i\nu(z-z')}dzdz', \qquad (6)$$

where $\hat{F}(z)$ denotes the Fourier transform[1] of $F(\nu)$, superscript c denotes complex conjugate, and the ensemble averages are defined in the same way that $\langle C(t,\mathfrak{I})\rangle$ is defined in Eq. (4). The mutual independence of L, T and E_0 has also been used.

Minimization of R^l involves the same principal difficulty encountered in Bayes estimation, namely that the distribution densities are not all known. In the case of $\tau(T)$, at least, there is often no satisfactory way to obtain a priori distributions from the physics of the problem. Furthermore, minimax estimation,[7] which is sometimes applicable in such situations, here leads to a trivial solution with no smoothing. Fortunately, there is a way of avoiding this difficulty if one invokes the ergodic hypothesis.[9] In essence this hypothesis permits replacement of ensemble averages by averages over the independent variable, i.e., time in the communications case and x-ray spectral frequency ν in the present

problem. However, a necessary condition for ergodicity is that the functions involved must be generated by a random stationary process, e.g., an x-ray spectrum with statistically uniform (a priori) structure characteristics for all spectral frequencies. It is immediately apparent that stationarity, i.e., statistical constancy, is an idealization never completely achieved in practice. Nevertheless it is possible to hypothesize a representative stationary process with statistical properties corresponding to those of a given nonstationary process at a certain value ν_0 of ν. The representative random stationary functions (RRSF) generated by the representative stationary process are useful in dealing with nonstationary functions in localized intervals of ν, since they have all of the convenient analytical properties associated with stationarity. For example, if $F(\nu_0,\nu)$ is an RRSF corresponding at ν_0 to the random function $F(\nu)$ generated by a nonstationary random process, then[10]

$$\langle \hat{F}(\nu_0,z)\ \hat{F}^c(\nu_0,z')\rangle = \hat{A}_F(\nu_0,z)\ \delta(z-z'), \tag{7}$$

where $\delta(z-z')$ is the Dirac delta function, $\hat{F}(\nu_0,z)$ is the Fourier transform in the generalized function sense of $F(\nu_0,\nu)$, and where $\hat{A}_F(\nu_0,z')$ is the Fourier transform on the variable $\nu-\nu'$ of the function $A_F(\nu_0,\nu-\nu')$ of $F(\nu_0,\nu)$ defined by

$$A_F(\nu_0,\nu-\nu') = \langle F(\nu_0,\nu)\ F(\nu_0,\nu')\rangle. \tag{8}$$

Also, it follows from the ergodicity of the representative process that the ensemble average in Eq. (8) is equivalent to an average over ν. Thus $A_F(\nu_0,\nu-\nu')$ is an autocorrelation function,[11] which can be related to sample properties of $F(\nu)$ through the RRSF.

One must now regard T and E_0 as functions generated by random, but not necessarily stationary, processes in ν. These functions are then approximated by their respective RRSF's at $\nu = \nu_0$ in Eq. (6) so that Eq. (7) is applicable to each. The function $L(\nu_0,\nu-\nu')$, already used to approximate $L(\nu,\nu-\nu')$ in Eq. (6), is a rather specialized RRSF at ν_0, since stationarity is implied by the fact that $L(\nu_0,\nu-\nu')$ is not explicitly dependent on ν. However, the association of L with a stationary process on $\nu-\nu'$ is difficult to justify in the presence of the physical evidence usually available. Ergodicity is therefore not invoked here, and Ω_L space must be constructed from physically probable smearing functions. The ensemble averages involving L must then be regarded as expectation values to be deduced from an experimental study of M, i.e., by a posteriori methods. In the RRSF approximation Eq. (6) becomes

$$R^l(\tau,\lambda,\delta) \cong \int_{-\infty}^{\infty} [\langle |\hat{V}(\nu_0,z)\hat{L}(\nu_0,z)-1|^2 \rangle \hat{A}_T(\nu_0,z) + |\hat{V}(\nu_0,z)|^2 \hat{A}_E(\nu_0,z)]dz, \tag{9}$$

where A_T and A_E are the autocorrelations of the RRSF's representing T and E_0, respectively. The right hand side of

Eq. (9) is a representative stationary risk: there is no explicit ν dependence, but in general the actual average risk is well approximated only in the immediate vicinity of $\nu = \nu_0$. Minimization with respect to V, which is now straightforward, leads to an optimum linear stationary estimator $V^b \ast 0$ for T with corresponding approximating properties, where

$$\hat{V}^b(\nu_0,z) = \frac{1}{\langle \hat{L}(\nu_0,z)\rangle} \times$$

$$\left[1 + \frac{\langle\, |\hat{L}(\nu_0,z)|^2\rangle - |\langle \hat{L}(\nu_0,z)\rangle|^2}{|\langle \hat{L}(\nu_0,z)\rangle|^2} + \frac{\hat{A}_E(\nu_0,z)}{\hat{A}_T(\nu_0,z)\,|\langle \hat{L}(\nu_0,z)\rangle|^2}\right]^{-1}. \tag{10}$$

Equation (10) is more general than its counterpart, Eq. (OPT-13), but also requires more detailed information for practical application. The first factor[12] characterizes the actual unfolding, while the second factor is associated with the smoothing or filtering. The product operation in Fourier space implies a convolution operation in direct space, although the inverse Fourier transform of the first factor ordinarily exists only as a generalized function.

The filtering factor in Eq. (10) contains three terms within the square brackets, the first of which is unity. The second term arises from E_M and is relatively independent of ν_0 when the explicit ν-dependence of L is slight. Nevertheless the second term achieves its greatest relative significance in spectral regions containing much structure. This follows from the form of the third term, which is essentially

a measure of the fluctuation amplitude of E_0 relative to that of T. The consequent possibility of a strong ν_0 dependence in the third term, i.e., nonstationarity, along with the general problem of extracting the necessary information concerning T, makes this term particularly subject to inaccurate evaluation. The remainder of the discussion is concerned almost exclusively with this evaluation problem.

If L is such that O may be satisfactorily represented by a RRSF, $\hat{A}_T(\nu_0,z)$ is obtainable in principle from $A_O(\nu_0,\nu-\nu')$, and $A_E(\nu_0,\nu-\nu')$, the autocorrelation functions of O and E, respectively, in the RRSF approximation.. One finds as a consequence of Eqs. (1) and (7),

$$\hat{A}_T(\nu_0,z) = \frac{\hat{A}_O(\nu_0,z)-\hat{A}_E(\nu_0,z)}{\langle |\hat{L}(\nu_0,z)|^2 \rangle}, \qquad (11)$$

where the assumed independence of T, L and E_0 and the assumption that $\langle E_O(\nu_0,\nu) \rangle = 0$ have been used. In consideration of practical difficulties in applying Eqs. (8) and (11) to samples of O and E_0, especially the difficulties resulting from nonstationarity, it is helpful to adopt simple models for T and E_0. This amounts to adopting definite functional forms for A_T and A_E, each having one or more adjustable parameters. These autocorrelation parameters then combine in the filtering factor of Eq. (10), where they appear simply as one or more filter parameters. Furthermore, by using model functions, the required averages over ν become much simpler to evaluate than the general form indicated in Eq. (8). An important

question, in view of nonstationarity, is that of the proper length of the ν-interval involved in these averages.

SAMPLE SPAN

An average over ν used to determine any $A_F(\nu_0, \nu-\nu')$ depends on the sample of $F(\nu)$ over an interval σ, called the sample span, rather than on the single point ν_0. Such an average therefore automatically assumes stationarity of $F(\nu)$ over σ. This assumption is emphasized in OPT by referring to σ as the stationarity region, but sample span is a more tangible concept. There are two basic principles which determine the proper σ:

(1) Appropriate Stationarity. The RRSF's of T and E_0 must properly represent these functions throughout, but not necessarily outside regions of ν involved in the convolutions implicit in Eq. (9). Otherwise the approximation of Eq. (9) becomes poor even at ν_0, and the derived V^b loses its validity.

(2) Adequate Sampling. A general nonstationary random function $F(\nu)$ and its RRSF are, by definition, statistically equivalent within any stationarity region of $F(\nu)$ which includes ν_0. Although the respective autocorrelation functions are therefore equivalent within σ, the sample span must include sufficient information on $F(\nu)$ for an adequate estimate of $A_F(\nu_0, \nu-\nu')$, the minimum σ being dependent on the autocorrelation characteristics of $F(\nu)$. When $F(\nu)$ is not sampled directly, it is the autocorrelation characteristics of the

function actually sampled which are significant. Thus in estimating A_T or its associated parameters from O, one must consider the characteristics of A_O, which in general is a broader function than A_T because of the smearing. Another aspect of sampling inadequacy concerns errors in the sample. As σ is reduced, the sample variance of A_F or its autocorrelation parameter(s) may be expected to increase because of the increased significance of experimental errors when averaging over less data.

The practical origin of these principles may be demonstrated by an example based on OPT. Here E_O is assumed to be uncorrelated between data points and to have zero expectation, so that A_E is essentially a delta function. Consequently, $\hat{A}_E$ is a constant,

$$\hat{A}_E(\nu_0,z) = \langle E_O^2(\nu_0,\nu)\rangle \Delta\nu, \tag{12}$$

where $\Delta\nu$ is the data interval. The model for T consists of a Poisson-distributed random array of spectral lines, each line having shape $I(\nu_0,\nu)$.[1] A derivation based on Eqs. (OPT-17), (OPT-20), and Eq. (7) gives

$$\hat{A}_T(\nu_0,z) = [n\langle a^2\rangle](\nu_0)\,|\hat{I}(\nu_0,z)|^2 + [n\langle a\rangle]^2(\nu_0)\,|\hat{I}(\nu_0,z)|^2\delta(z), \tag{13}$$

where n denotes the average number of lines per unit frequency interval and a is the random area under any line. Both n and a, as well as the line shape may be regarded as nonstationary in ν. The second term of Eq. (13) is irrelevant,

except insofar as the normalization of V^b is concerned, so that for a given $I(\nu_0,\nu)$ the relevant statistical properties of T are completely characterized by the single autocorrelation parameter $[n\langle a^2\rangle](\nu_0)$. By combining Eqs. (11) to (13) and solving for this parameter in terms of $A_O(\nu_0,0)$ and $A_E(\nu_0,0)$, one obtains with the help of Eq. (8)

$$[n\langle a^2\rangle](\nu_0) = \frac{\langle O^2(\nu_0,\nu)\rangle - \langle O(\nu_0,\nu)\rangle^2 - \langle E_O^2(\nu_0,\nu)\rangle}{\int_{-\infty}^{\infty} |\hat{I}(\nu_0,z)|^2 \langle |\hat{L}(\nu_0,z)|^2\rangle \, dz}, \qquad (14)$$

which is a more general form of Eq. (OPT-14). Values of the parameter $[n\langle a^2\rangle](\nu_0)$ as a function of the sample span σ are shown in Fig. (4) for three different situations involving Lorentzian line spectra, as illustrated schematically in the insets, where the solid circle represents $O(\nu_0)$. Two curves are shown. The dashed curve represents actual values of $n\langle a^2\rangle$ averaged over σ. This ideal curve is derived from the number of lines included within σ and their underlying areas, which are generally not known in an actual practical problem. The solid curve represents the approximation to the dashed curve obtained by applying Eq. (14) to a sample of $O(\nu)$ extending over the span σ, just as in a practical problem, but with L given and the $\langle E_O^2\rangle$ term neglected for simplicity. The behavior of the dashed curve in the top example illustrates the appropriate stationarity principle most effectively. With σ too large

the assumed stationarity is excessive and $n\langle a^2\rangle$ is too small for optimum smoothing. This is a result of representing the average behavior of T over too large a region, much of which is irrelevant to behavior near ν_0. In this case V^b oversmoothes. On the other hand, as σ approaches zero, the actual $n\langle a^2\rangle$ approaches infinity, and the corresponding V^b eventually undersmoothes. The difficulty here is that, with σ too small, the apparent behavior of T is not characteristic of the entire region involved in the unfolding. In the center and bottom examples an oversmoothing occurs when σ is too small. Here, the actual value of $n\langle a^2\rangle$ may not indicate the presence of adjacent lines, in which case a V^b based on the dashed curve smoothes over too wide a range. This range may in fact include the adjacent lines and thus distort the solution at ν_0. The solid curve, representing values of $n\langle a^2\rangle$ on which V^b is based in practice, is also subject to the appropriate stationarity principle insofar as it approximates the dashed curve. However, an additional limitation on σ is introduced in the failure of the approximation at small σ, particularly when ν_0 is near a line peak. Fortunately, the failure of the approximation is normally such as to compensate for the stationarity limitation at small σ, although this compensation is often too large. This is evident to the extreme in the top example where the infinite divergence of the dashed curve is nullified in the solid curve, and to a lesser extent in the other two examples where the indication of adjacent lines is extended to smaller values of σ.

Errors in the solid curve associated with nonzero values of E_0 are ordinarily present but are not indicated in Fig. 4. Their possible significance at small σ is evident, however, particularly in the center example.

The effect of the two principles in terms of the unfolded spectrum is illustrated in Fig. (5). Here the example of Figs. (1) and (2), where the observed half-width γ at half-maximum equals twice the true half-width β, is unfolded using different sample spans. The points labelled OPT solution correspond to the value $\sigma_{90\%}$ of Fig. (4), i.e., $\sigma = 12.6\gamma$, which is the value given by the 90% limit criterion of OPT. The curve labelled overstationary solution corresponds to a σ which is ten times greater, and thus amplifies the smoothing deficiencies of OPT apparent in Figs. (1) and (2). These deficiencies are related almost entirely to excessive stationarity as discussed in connection with the top example of Fig. (4), which explains the oversmoothing at the peak. A similar argument applied to the center example of Fig. (4) explains the undersmoothing in the tail. The curve labelled undersampled corresponds to a value of σ which is one-tenth of $\sigma_{90\%}$. This is in the region of σ where the solid curve of Fig. (4) may depart strongly from the dashed. The oversmoothing at the peak in this case is therefore to be expected on the basis of inadequate sampling. The tail region of the undersampled curve, however, shows certain desirable properties, such as substantial fall-off in the noise level and

relative freedom from oscillations. This is not surprising in view of the substantial agreement between solid and dashed curves in the center example of Fig. (4), and because the sampling in this instance tends to compensate for insufficient stationarity. Spurious oscillations in the tail region often accompany overstationarity, and are produced by inadequate explicit ν-dependence of the unfolding operator V, which in general is an oscillating function of $\nu-\nu'$.

REFINEMENTS

It is evident from the preceding discussion that no single value of σ can produce uniformly good results under all conditions. Usually, some improvement over OPT may be achieved by reducing the sample span to σ_p, corresponding to the maximum of the solid curve in the top example of Fig. (4). Even this peak criterion, however, which minimizes the smoothing at the line peaks, does not alone solve the problem of oversmoothing in such regions. In fact, when the observed spectral lines are Lorentzian, σ_p equals 7.0γ and the improvement over using $\sigma_{90\%} = 12.6\gamma$ is rather small, although it becomes quite significant for Gaussian, and for some other non-Lorentzian shapes. Although apparently rare in practice, it seems impossible to completely exclude situations where the appropriate stationarity principle, rather than inadequate sampling, becomes the limiting factor at small, as well as at large σ. In such cases the peak criterion should produce

both insufficient smoothing near line peaks and oversmoothing in the tails. Some superseding criterion would then be required, such as an ultimate lower limit on σ or limits on the filter parameter(s). Normally, however, further improvement requires the possibility of sample spans less than σ_p. This possibility is frustrated, as we have seen, by the principle of adequate sampling when applied to the observed spectrum. Apparently one can relax this restriction somewhat by sampling a function whose autocorrelation function is less broad, e.g., the true spectrum. This suggests an unfolding operation on $O(\nu)$ before sampling. Preliminary unfolding is also indicated in situations where representation of O by an RRSF is inappropriate, so that Eqs. (11) or (14) cannot be used. An example is where L is a step function, thus making O the indefinite integral of T. Even if T is a stationary process in this case, O is strongly nonstationary since its expectation value changes monotonically with ν. This example occurs in practice in the unfolding of electron energy-loss spectra by the retarding field method.[4]

Consider now the possibility of determining $n\langle a^2\rangle$ by sampling a spectrum other than $O(\nu)$ from which $\langle L\rangle$ has been unfolded; or better still, from which has been unfolded $\langle L\rangle * T$, the full observed line-shape function.[13] The latter approach makes more effective use of the a priori information, but also places somewhat greater demands on the validity of

the model, including the inherent line-shape function $I(\nu_0,\nu)$. For example, such a spectrum is obtained by applying to O the preliminary linear unfolding operator Q defined by

$$\hat{Q}(\nu_0,z) = \frac{1}{\langle \hat{L}(\nu_0,z)\rangle \hat{I}(\nu_0,z)} \times \tag{15}$$

$$\left[1+\frac{\langle |\hat{L}(\nu_0,z)|^2\rangle - |\langle \hat{L}(\nu_0,z)\rangle|^2}{|\langle \hat{L}(\nu_0,z)\rangle|^2}+\frac{q(\nu_0)}{|\hat{I}(\nu_0,z)\langle \hat{L}(\nu_0,z)\rangle|^2}\right]^{-1};$$

$$z \neq 0.$$

The smoothing factor here is of the form occurring in V^b when the OPT model is used, i.e., of the form appearing in Eq. (10) when Eqs. (12) and (13) are used, with $\langle E_0^2\rangle \Delta\nu/[n\langle a^2\rangle]$ replaced by the preliminary smoothing parameter q. Equation (14) is now replaced by

$$[n\langle a^2\rangle](\nu_0) = \tag{16}$$

$$\frac{\langle [Q*O(\nu_0,\nu)]^2\rangle - \langle Q*O(\nu_0,\nu)\rangle^2 - \langle E_0^2(\nu_0,\nu)\rangle \Delta\nu \int_{-\infty}^{\infty} |\hat{Q}(\nu_0,z)|^2 dz}{\int_{-\infty}^{\infty} |\hat{Q}(\nu_0,z)\hat{I}(\nu_0,z)|^2 \langle |\hat{L}(\nu_0,z)|^2\rangle dz}.$$

This expression relates the autocorrelation parameter which characterizes T to the preliminarily unfolded spectrum Q*O. One now uses Eq. (16) to prescribe the values of $n\langle a^2\rangle$ to use in the final optimum unfolding operator V^b. The dependence of $n\langle a^2\rangle$ on E_M, as well as on E_0, becomes more apparent if the integral in the denominator of Eq. (16) is expressed in terms of $|\langle \hat{L}(\nu_0,z)\rangle|^2$ plus a correction term. Generally both E_0

and E_{ij} correction terms, especially the former, become more significant as $q(\nu_0)$ is decreased. The minimum q is thus governed by the uncertainty associated with E_0 and E_M and by variance limitations imposed on $n\langle a^2\rangle$ in accordance with the adequate sampling principle state above. If the peak criterion for σ is applied to the preliminarily unfolded spectrum, a definite relationship exists between σ_p and the minimum q for a given observed line shape. Thus σ is again limited by the adequate sampling principle, but now only by the sample-error aspect of this principle. The limitation on σ here is of a fundamental nature, since it depends ultimately on the experimental errors and not on autocorrelation characteristics, which can be varied by preliminary unfolding. The broadness of the autocorrelation function characterizing $Q\neq 0$ depends on q and hence is also limited by E_0 and E_M.

Figure 6 compares a solution obtained using preliminary unfolding, designated as refined OPT solution, with the original OPT solution of Figs. (1) and (2). The preliminary smoothing parameter $q(\nu_0)$ was chosen at each point of the curve to correspond to a 20% relative rms error $[E_m\langle a^2\rangle]$ in the value of $n\langle a^2\rangle$ as obtained from Eq. (16). The corresponding rms error in the solution is thereby restricted to about 10% or less of the rms error arising directly from the E_0 noise, which is indicated in the figure. The relationship between $q(\nu_0)$ and $[E_r n\langle a^2\rangle]$ was based on the simultaneous solution of the following approximate equations[14]

$$[E:n\langle a^2\rangle](\nu_0) \cong \frac{\left(\frac{\Delta\nu}{T}\right)\left[\frac{Q*O(\nu_0)}{\gamma}\right]^{-3/2}\,[q(\nu_0)]^{-1}\,\langle E_O^2(\nu_0,\nu)\rangle}{\langle[Q*O(\nu_0,\nu)]^2\rangle - \langle Q*O(\nu_0,\nu)\rangle^2}, \tag{17}$$

$$\frac{\sigma_P(\nu_0)}{\gamma} \cong \frac{19}{-\ell n\ q(\nu_0)} + 0.1. \tag{18}$$

Values of σ_P range from 1.5γ at the peak of the curve to 2γ at $\nu = 5\beta$ in the tail. Preliminary unfolding on the basis of a fixed $[E:n\langle a^2\rangle]$ thus not only permits a reduction of σ, but provides the additional flexibility of a variable σ as well. The refined optimized solution of Fig. 6 represents about the best solution possible with a one-parameter linear filter based on the level of a priori information assumed here. Even here, the true curve does not always fall within the rms noise associated with the corrected curve. However, with the quadratic cost function used here the total rms error is given by the square root of the average risk R^l (c.f. Eq. (6)), which includes the anticipated distortion or smoothing error.[1] When this is taken into consideration the rms error limits of the refined optimum solution either include the true curve or come very close to it at all points. This ability to estimate total error from the risk represents another important advantage of the OPT approach.

At this stage one can only speculate on the capabilities of more general types of optimum filters. Also uncertain is the improvement possible by abandoning the RRSF approximation

in favor of an analysis in terms of nonstationary processes. However, in view of the ultimate limitation on sampling accuracy by experimental errors, it seems doubtful whether the practical gain would justify the loss in mathematical simplicity. From a practical standpoint the most fruitful area for further development probably lies in better formulation of the a priori information. One cannot, for example, expect true optimization when the relatively simple model of OPT provides a poor representation of the true spectrum. Generally, for sharp spectral features such as lines and absorption edges one can expect an optimum correction of the sort demonstrated in the figures. On the other hand, for slowly varying bands or other broad features there is a tendency toward undersmoothing and an associated overestimate of the error. This effect is perceptible in Fig. 6 in the remote tail of the spectral line. Sophisticated models in the form of detailed physical theories would undoubtedly yield the best results provided they are in fact realistic. The information gained from experiment in such cases is, of course, correspondingly diminished.

CONCLUSIONS

When compared on the basis of both variance and expectation value, optimized unfolding is capable of producing solutions which are significantly superior to those produced by other methods. This is especially true when the unfolding correction is large. Nonstationarity is an important

factor in optimized unfolding and accounts to a large extent for such difficulties as distortion (oversmoothing) of line peaks, excessive noise fluctuations (undersmoothing) in line tails, and spurious oscillations near large changes in spectral intensity. Proper allowance for nonstationarity is normally limited by the large sample span required for adequate determination of the local statistical character of the true spectrum. This limitation is especially pronounced when the determination is made directly from samples of the observed spectrum, even when extended by a new criterion for the sample span which minimizes smoothing of the line peaks. Additional flexibility of the sample span and compensation for nonstationarity can be achieved by including the extra step of preliminary unfolding before sampling. An ultimate limit to this approach is the fundamental one imposed by experimental uncertainties. Preliminary unfolding also provides a means of sampling which is compatible with integrated spectra.

APPENDIX

The approximation expressed in Eq. (2) is obtained by expanding $L \equiv M-E_M$ in partial derivatives $L_\nu^{(n)}$ with respect to the explicit ν-dependence, holding the translational variable $\nu-\nu'$ constant, i.e.,

$$L_\nu^{(n)} \equiv \left(\frac{\partial^{(n)} L(\nu,\nu-\nu')}{\partial \nu^{(n)}}\right)_{\nu-\nu'}. \tag{19}$$

Rewriting Eq. (1) in terms of such an expansion about the point $\nu = \nu_0$, and linearly operating with an unspecified function $V(\nu_0,\nu-\nu'')$ gives

$$\begin{aligned}
&\int_{-\infty}^{\infty} V(\nu_0,\nu-\nu'')\ [O(\nu'')-E_O(\nu'')]\,d\nu'' = \\
&\int_{-\infty}^{\infty}\int_{-\infty}^{\infty} V(\nu_0,\nu-\nu'')\ L(\nu_0,\nu''-\nu')\ T(\nu')\,d\nu'\,d\nu'' \\
&+ \int_{-\infty}^{\infty}\int_{-\infty}^{\infty} V(\nu_0,\nu-\nu'')(\nu''-\nu_0)L_\nu^{(1)}(\nu_0,\nu''-\nu')T(\nu')\,d\nu'\,d\nu'' \\
&+ \ldots .
\end{aligned} \tag{20}$$

If L is such that T is uniquely determined by $O-E_O$ and if V is defined as a generalized function by its Fourier transform with respect to the translational variable,

$$\hat{V}(\nu_0,z) = \left[\int_{-\infty}^{\infty} L(\nu_0,\nu)\ e^{-2\pi i\nu z}\ d\nu\right]^{-1}, \tag{21}$$

then the zeroth order term on the right hand side of Eq. (20) is equal to $T(\nu)$.[1] Setting $\nu_0 = \nu$ and neglecting the contribution of the higher order terms gives Eq. (2). Substitution of the solution given by Eq. (2) into the higher order terms of Eq. (20) gives an estimate of the error in the approximation.

ACKNOWLEDGMENTS

The author is grateful to Lorenz Y. Lipton for performing computer computations required for Fig. (6). The invaluable assistance of Dr. D. E. Zilmer in reviewing the manuscript is also acknowledged.

FOOTNOTES

[1] J. O. Porteus, J. Appl. Phys. 33, 700 (1962).

[2] I. Y. Nikiforov, V. P. Sachenko, M. A. Blokhin, Bull. Acad. Sci. USSR, Phys. Ser. 25, 1057 (1961).

[3] William C. Sander, J. Appl. Phys. 37, 1495 (1966).

[4] J. O. Porteus, in Atomic Collision Processes (North-Holland Publishing Company, Amsterdam, 1964), p. 77.

[5] P. H. van Cittert, Z. Physik 79, 722 (1932).

[6] V. P. Sachenko, Bull. Acad. Sci. USSR, phys. Ser. 25, 1052 (1961).

[7] David Middleton, An Introduction to Statistical Communication Theory (McGraw-Hill Book Company, Inc., New York, 1960), Part 4.

[8] David Middleton, An Introduction to Statistical Communication Theory (McGraw-Hill Book Company, Inc., New York, 1960), pp. 787, 791.

[9] David Middleton, An Introduction to Statistical Communication Theory (McGraw-Hill Book Company, Inc., New York 1960), p. 56.

[10] R. L. Stratonvich, Topics in the Theory of Random Noise Vol. I (Gordon and Breach Science Publishers, Inc., New York, 1963), pp. 23, 27, 28.

[11] David Middleton, An Introduction to Statistical Communication Theory (McGraw-Hill Book Company, Inc., New York, 1960), Sec. 3.1.

[12] Observe that $\langle L(\nu_0,s)\rangle$ is not necessarily equal to $M(\nu_0,s)$, but depends in general on the form of the distribution density $W_M(M-L)$. A simple example is where $M(\nu_0,\nu-\nu')$ is Lorentzian, corresponding to the smearing associated with short-lived x-ray excited state, but has an uncertain width parameter β. In this case the L's belonging to Ω_L space are also Lorentzian, but $\langle L\rangle$ as determined from the distribution density of β generally has a slightly different functional form, which approaches pure Lorentzian only as the uncertainty in β vanishes.

[13] The usual objection that unfolding the full line shape leads to an infinite risk, i.e., to an infinite $\langle L_t^2\rangle$ for the unfolded spectrum, is not pertinent if the preliminarily unfolded spectrum is used only to determine $[n\langle a^2\rangle](\nu_0)$.

[14] Equation (17) is derived from Eq. (16) under the following assumptions: Lorentzian observed line shape with half-width γ at half maximum, $E_M = 0$, $\Delta\nu/\gamma \ll 1$, $\sigma/\gamma \gg 1$. If the last assumption is not strictly satisfied, Eq. (17) tends to overestimate the error somewhat. Equation (18) results from application of the peak criterion for σ to the preliminary unfolded spectrum, assuming Lorentzian observed line shape and $10^{-3} < q < 10^{-2}$.

FIGURE CAPTIONS

Fig. 1. Comparison in a simple example of unfolded spectra, as given by the optimized method of the author and the iterated convolution method of van Cittert. For the latter method the expectation curve is shown only in the fifth order of approximation. Expectation values corresponding to lower orders are indicated at isolated points by open circles. Vertical bars indicate the rms noise levels of the various solutions in relation to the input rms noise level of the observed spectrum. The relationship of true to observed spectrum is shown schematically in the inset.

Fig. 2. Comparison in the simple example of Fig. 1 of unfolded spectra as given by the optimized method of the author and the derivative method of Sachenko. In the latter method the expectation curve corresponds to a data interval of 0.7β, which excludes differences of order larger than the sixth. An arbitrary smooth curve has been fitted to the calculated points, thus reducing somewhat the effect of discontinuities resulting from changes in the order of approximation. Vertical bars indicate the rms noise levels of the solutions in relation to the input rms noise level of the observed spectrum.

Fig. 3. Schematic relationship of function spaces and decision rule in the unfolding problem.

Fig. 4. Demonstration of the two principles which determine the sample span σ for three different situations involving Lorentzian line spectra. The solid circle in the inset indicates in each case the particular observed data point $O(\nu_0)$ to be corrected. The dashed curve, which represents actual values of $n\langle a^2\rangle$ averaged over the interval σ, governs the determination of σ on the basis of stationarity alone. This curve approaches infinity in the top example and peaks at 1.15 on the ordinate scale of the bottom example. The solid curve, which shows values of $n\langle a^2\rangle$ obtained from σ-interval samples of $O(\nu)$, as in practice, governs the determination of σ on the basis of both appropriate stationarity and adequate sampling as explained in the text. The values of σ designated by the subscripts 90% and P are those which correspond, respectively, to the 90% limit criterion at OPT and to the peak criterion of the present work.

Fig. 5. Improperly unfolded spectra, again using the simple example of Fig. 1. The long-dashed curve violates the appropriate stationarity principle, while the short-dashed curve violates the adequate sampling principle. The solution given by the optimized method of the author (solid circles) is included for comparison. Vertical bars again indicate rms noise levels.

Fig. 6. Comparison of the original OFT solution with an OFT solution refined by preliminary unfolding before sampling, and use of the peak criterion for σ. The basis for comparison is the example of Fig. 1. Points of the iterative convolution solution (fifth order approximation) and derivative solution are also shown for comparison.

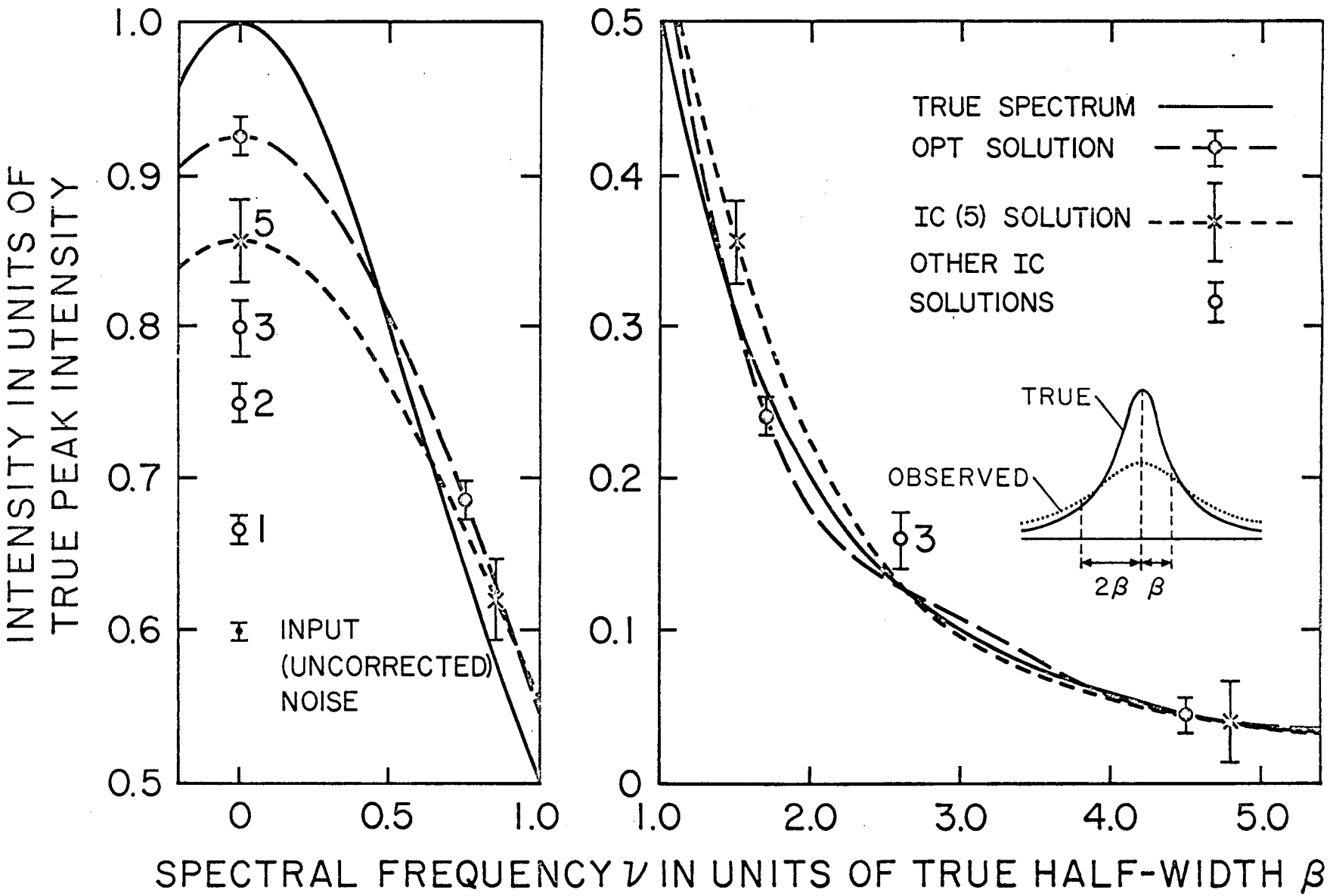
INTENSITY IN UNITS OF TRUE PEAK INTENSITY
1.0
0.9
0.8
0.7
0.6
0.5
0
0.5
1.0
5
3
2
1
INPUT (UNCORRECTED) NOISE
0.5
0.4
0.3
0.2
0.1
0
1.0
2.0
3.0
4.0
5.0
3
TRUE SPECTRUM
OPT SOLUTION
IC (5) SOLUTION
OTHER IC SOLUTIONS
TRUE
OBSERVED
2β
β
SPECTRAL FREQUENCY ν IN UNITS OF TRUE HALF-WIDTH β

FIG. 1

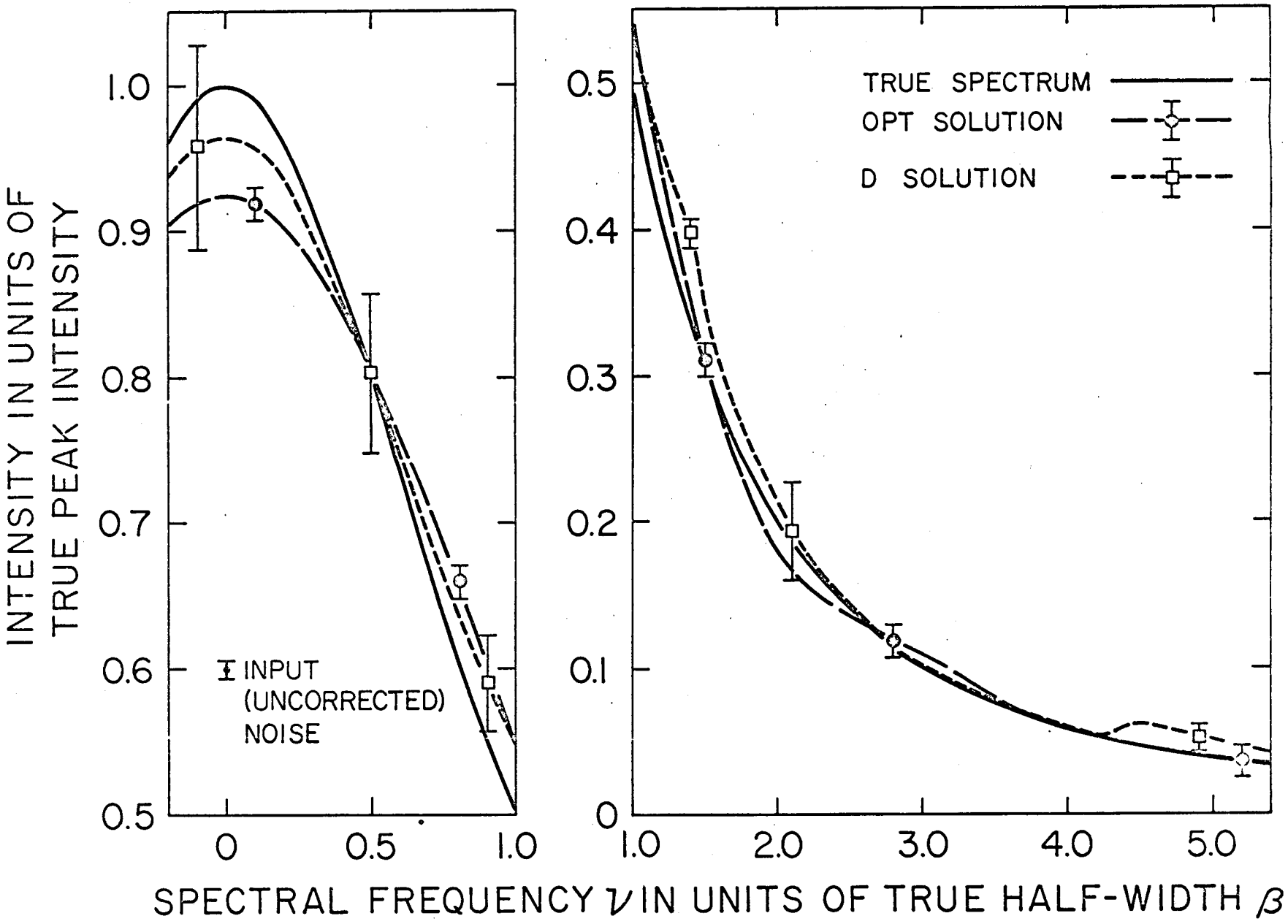
INTENSITY IN UNITS OF TRUE PEAK INTENSITY
1.0
0.9
0.8
0.7
0.6
0.5
0
0.5
1.0
INPUT (UNCORRECTED) NOISE
0.5
0.4
0.3
0.2
0.1
0
1.0
2.0
3.0
4.0
5.0
TRUE SPECTRUM
OPT SOLUTION
D SOLUTION
SPECTRAL FREQUENCY ν IN UNITS OF TRUE HALF-WIDTH β

FIG. 2

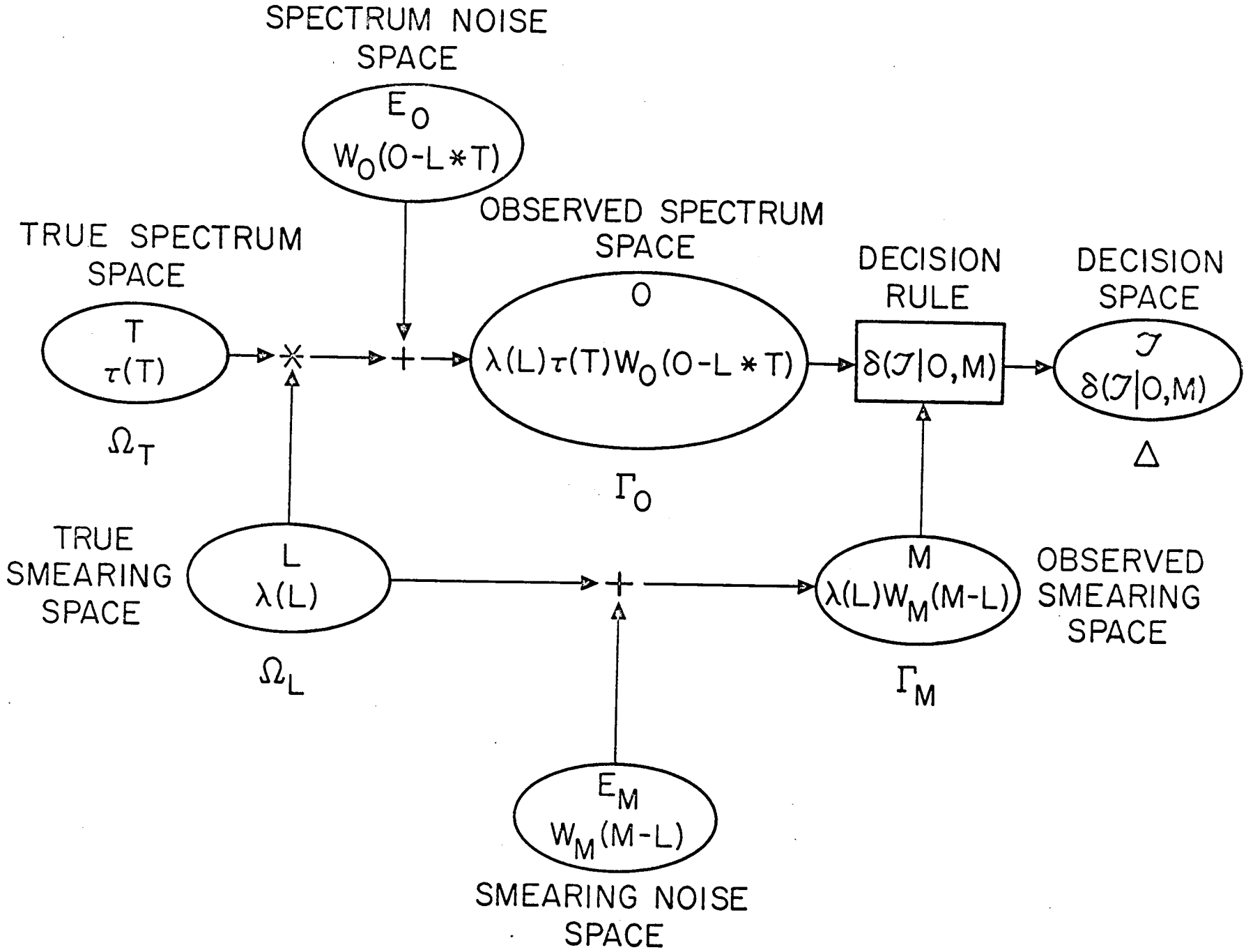
SPECTRUM NOISE SPACE
E_0
$W_0(O-L*T)$
TRUE SPECTRUM SPACE
T
$\tau(T)$
Ω_T
OBSERVED SPECTRUM SPACE
O
$\lambda(L)\tau(T)W_0(O-L*T)$
Γ_O
DECISION RULE
$\delta(\mathcal{J}|O,M)$
DECISION SPACE
$\mathcal{J}$
$\delta(\mathcal{J}|O,M)$
Δ
TRUE SMEARING SPACE
L
$\lambda(L)$
Ω_L
M
$\lambda(L)W_M(M-L)$
Γ_M
OBSERVED SMEARING SPACE
E_M
$W_M(M-L)$
SMEARING NOISE SPACE

FIG. 3

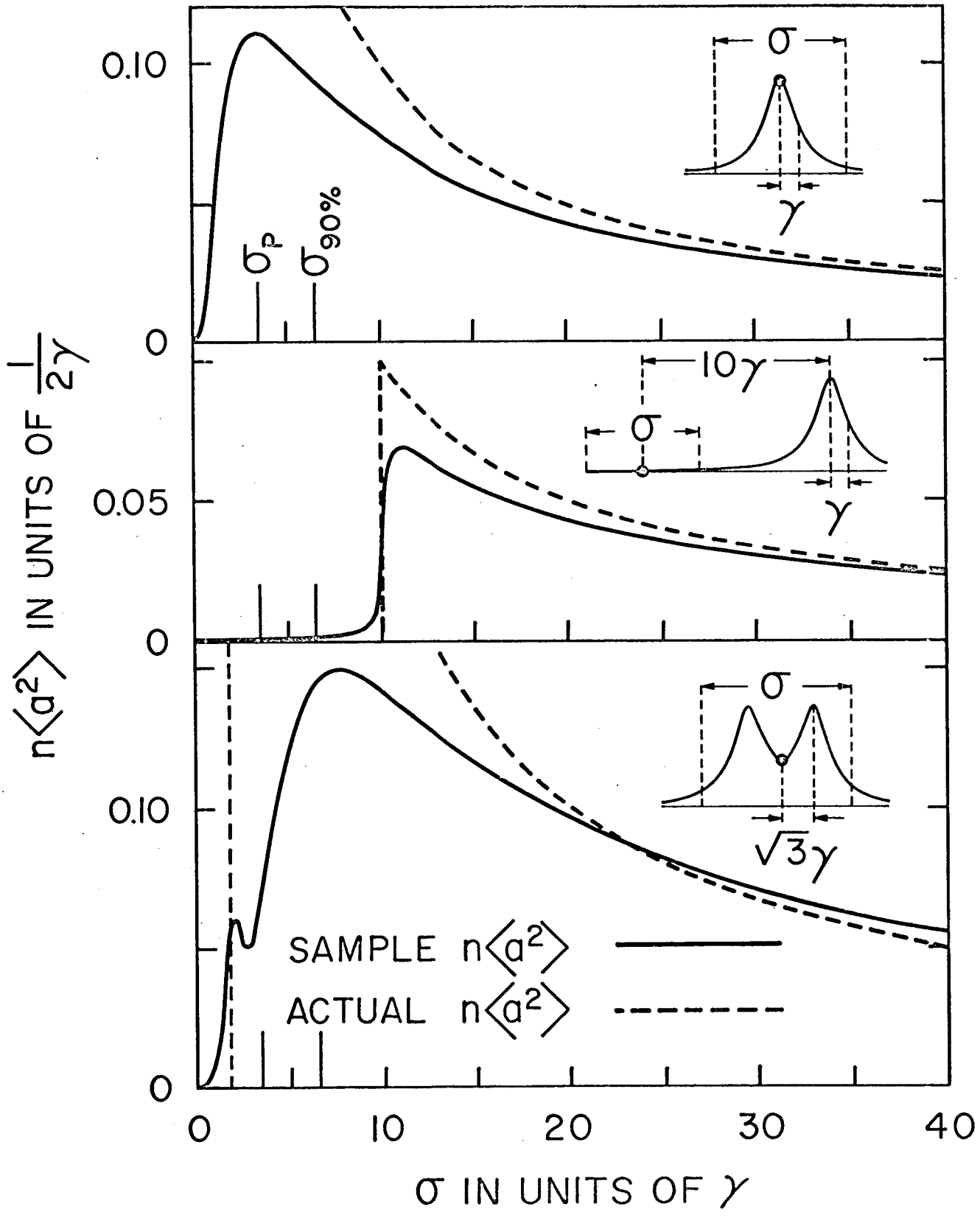
0.10
0
0.05
0
0.10
0
$n\langle a^2\rangle$ IN UNITS OF $\frac{1}{2\gamma}$
σ_p
$\sigma_{90\%}$
σ
γ
10γ
$\sqrt{3}\gamma$
SAMPLE $n\langle a^2\rangle$
ACTUAL $n\langle a^2\rangle$
0
10
20
30
40
σ IN UNITS OF γ

FIG. 4

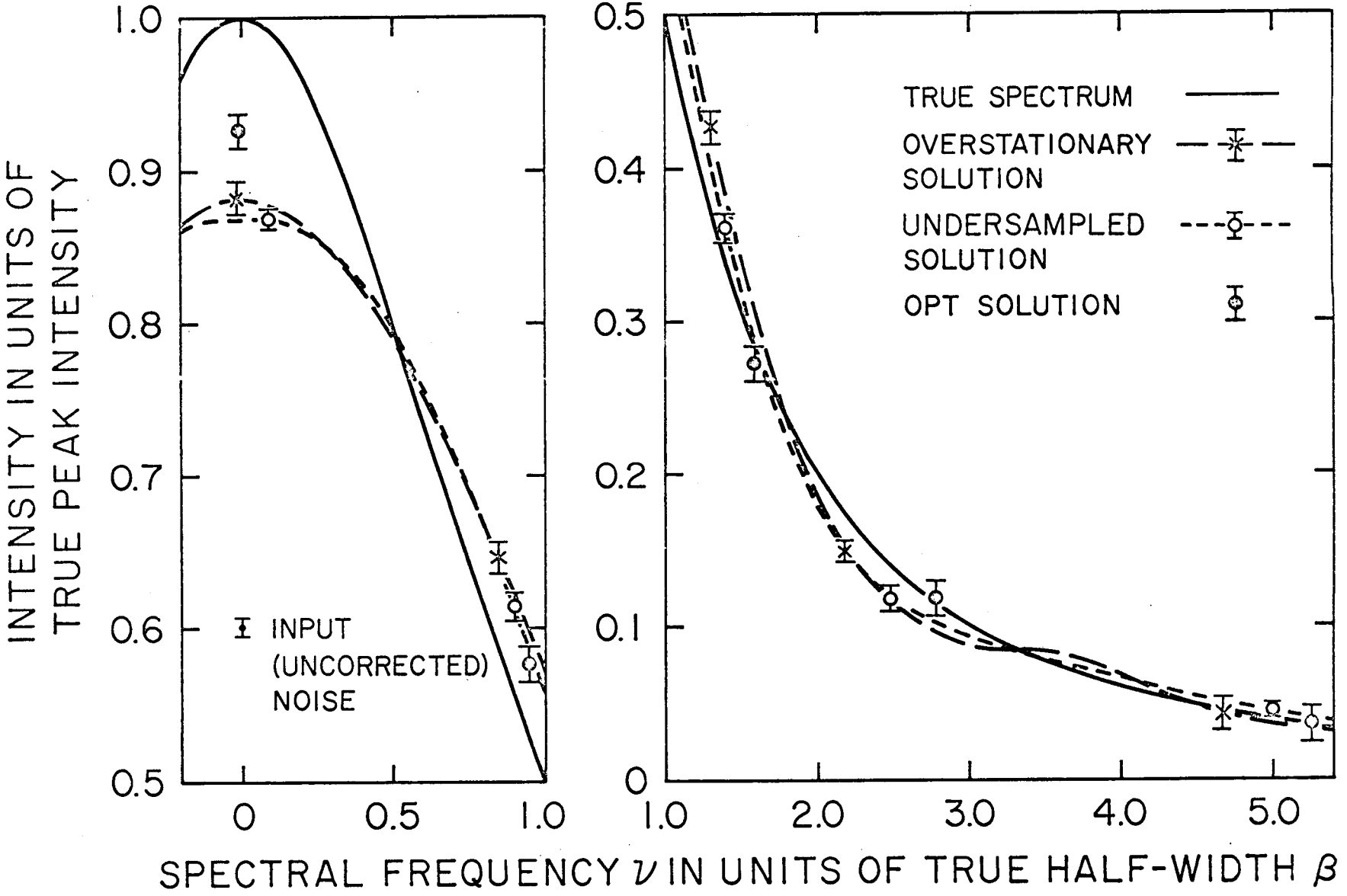
INTENSITY IN UNITS OF TRUE PEAK INTENSITY
1.0
0.9
0.8
0.7
0.6
0.5
0
0.5
1.0
INPUT (UNCORRECTED) NOISE
0.5
0.4
0.3
0.2
0.1
0
1.0
2.0
3.0
4.0
5.0
TRUE SPECTRUM
OVERSTATIONARY SOLUTION
UNDERSAMPLED SOLUTION
OPT SOLUTION
SPECTRAL FREQUENCY ν IN UNITS OF TRUE HALF-WIDTH β

FIG. 5

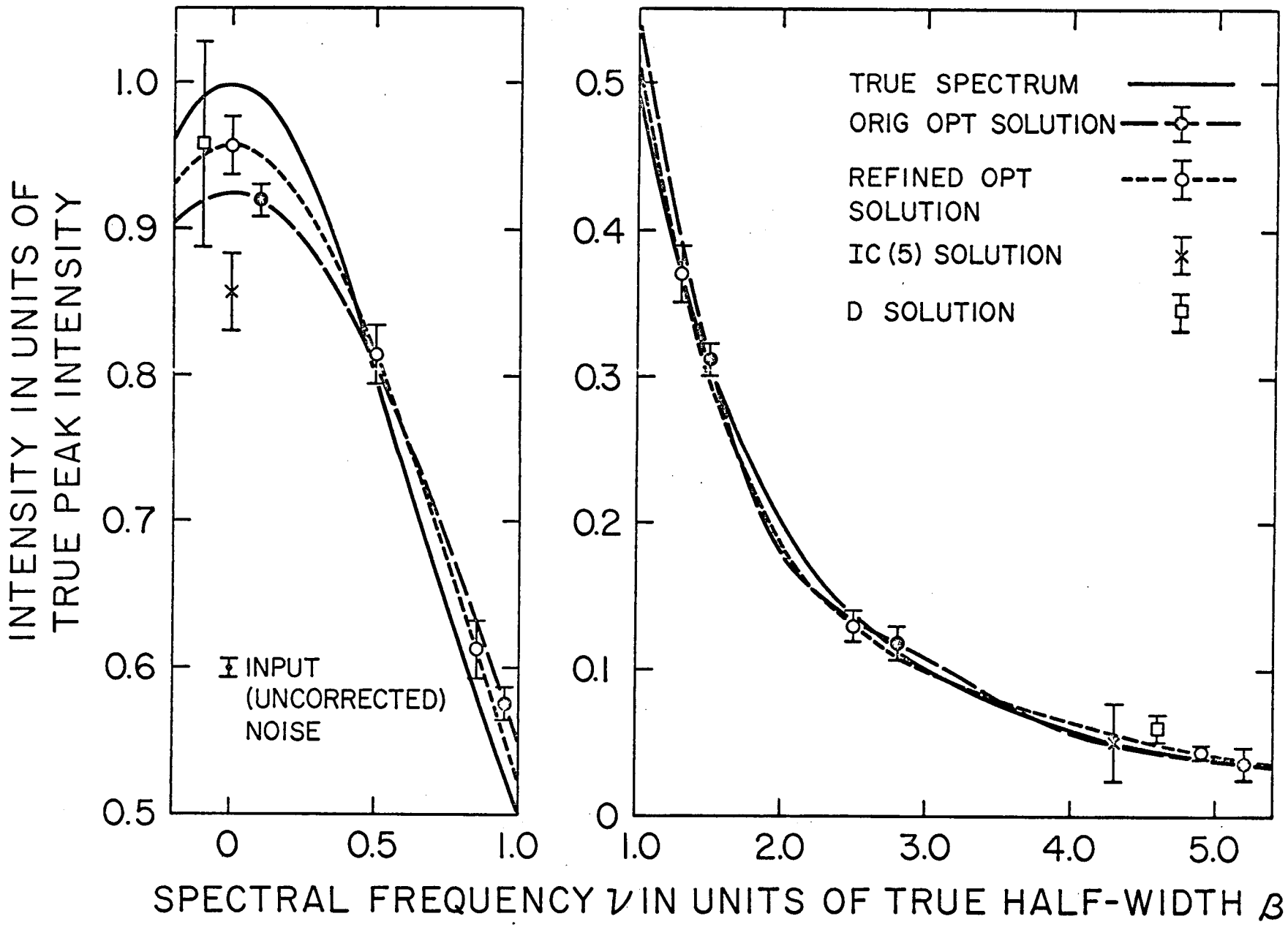
INTENSITY IN UNITS OF TRUE PEAK INTENSITY
1.0
0.9
0.8
0.7
0.6
0.5
0
0.5
1.0
INPUT (UNCORRECTED) NOISE
0.5
0.4
0.3
0.2
0.1
0
1.0
2.0
3.0
4.0
5.0
TRUE SPECTRUM
ORIG OPT SOLUTION
REFINED OPT SOLUTION
IC (5) SOLUTION
D SOLUTION
SPECTRAL FREQUENCY ν IN UNITS OF TRUE HALF-WIDTH β

FIG. 6